IEEE Access
Multidisciplinary | Rapid Review | Open Access Journal

Received August 16, 2018, accepted September 19, 2018, date of publication October 1, 2018, date of current version October 29, 2018.

Digital Object Identifier 10.1109/ACCESS.2018.2872696

Monolithically 3-D Printed Hemispherical Resonator Waveguide Filters With Improved Out-of-Band Rejections

JIN LI[1], (Member, IEEE), CHENG GUO[2], LIJIAN MAO[3], JIE XIANG[4], GUAN-LONG HUANG[1,5], (Member, IEEE), AND TAO YUAN[1]

[1]ATR National Key Laboratory of Defense Technology, College of Information Engineering, Shenzhen University, Shenzhen 518060, China
[2]Department of Electronic, Electrical and Systems Engineering, University of Birmingham, Birmingham B15 2TT, U.K.
[3]Kunshan Tongxin Surface Science and Technology Co., Ltd., Kunshan 215316, China
[4]Shanghai New East China Institute of Optoelectronic Technology, Shanghai 201114, China
[5]State Key Laboratory of Millimeter Waves, Nanjing 210096, China

Corresponding author: Guan-Long Huang (guanlong.huang@szu.edu.cn)

This work was supported in part by the National Natural Science Foundation of China under Grant 61701320 and Grant 61801300, in part by the Shenzhen Science and Technology under Grant JCYJ20170818101347761, in part by the State Key Laboratory of Millimeter Waves under Grant K201932, and in part by the New Teacher Natural Science Research Project of Shenzhen University under Grant 2018078.

ABSTRACT This paper provides a comprehensive presentation for the RF design and implementation of novel millimeter-wave waveguide bandpass filters (BPFs) that are composed of compact hemispherical resonators. The proposed hemispherical resonator features a high unload quality factor and a volume 50% smaller than a spherical one and more significantly is much less degenerate than the latter due to its structural asymmetry. With proper geometrical configurations, the hemispherical resonator BPF can perform significantly improved out-of-band rejections compared with the spherical resonator BPFs of the same orders. The second- and fourth-order waveguide-fed BPFs are designed at *X* and *Ka* bands with flexible inter-resonator coupling geometries. The proof-of-concept *Ka*-band filters are monolithically prototyped with a high-temperature-resistant ceramic-filled photosensitive resin by using a fast and low-cost stereolithography (SLA)-based additive manufacturing technique. A proprietary electroless nickel/copper/silver plating process is reported for surface metallization of the utilized commercially available resin. The *Ka*-band filters demonstrate in the passbands small insertion losses (0.43–1 dB), good return losses (mostly >10–17 dB), and small frequency shifts (0.01%–0.47%), which validates excellent fabrication accuracy and reliability of the SLA printing and the metal plating. Characterization and quantification of surface morphology for SLA-printed samples are performed by employing contact profilometry and scanning electron microscopy.

INDEX TERMS Additive manufacturing, bandpass filter, hemispherical resonator, monolithic, stereolithography, surface roughness, 3-D printed, waveguide filter.

I. INTRODUCTION

Modern trends of research and development in multiband and multifunctional operability for RF front-ends have brought about ever-increasingly complicated physical geometries and system architectures of the front-end hardware. Usually, the involved cavity and waveguide components are implemented with metallic building materials by using typical subtractive manufacturing technologies such as computer-numerical-controlled (CNC) milling. In spite of many attractive attributes such as high fabrication accuracy, small surface roughness, and mechanical robustness of the CNC-milled parts, several practical limitations are worth being noticed. In the first place, flexible high-precision multi-axis CNC milling machines may not be easily available. Some geometrically complex structures can be milled out, but at expense of a high fabrication cost and a long lead time, whereas some others cannot be milled monolithically. Their electronic models have to be split into multiple pieces for milling individually, which requires for the finished parts a labor-intensive post-fabrication assembly involving precise alignment, fastening, and tuning. The misalignment and cutting among these split blocks may result in undesired RF-performance degradation, particularly for the devices operating in higher millimeter-wave to terahertz frequencies.

In addition, the engineered systems can be bulky due to a large amount of redundant building material that cannot be easily milled away, which is not preferred in the applications where a miniaturized volume and a light weight are of major concern.

In recently years, emerging additive manufacturing (AM) technology, also known as three-dimensional (3-D) printing, has attracted numerous research interests in RF engineering fabrications. 3-D printing presents attractive benefits over conventional subtractive manufacturing technologies such as an enhanced flexibility in structural design and material selection for the devices, a possibility of consolidating multiple devices into one single part for fabrication, and a significant reduction in lead time, cost, and material wastage. These advantages have made 3-D printing an alternative pathway for rapid prototyping microwave front-end passive components such as waveguides, filters, antennas, and their associated feeding networks. An overview expounding classifications, technical principles, and material properties of universal AM techniques to date has been reported in [1]. For the fabrication of waveguide components, these printing techniques can be divided into two distinct approaches based on the printing material properties. One approach is directly printing the structure by laser-sintering/melting metallic powders (e.g., [2]–[4]). Such devices can be immediately operational after being printed and polished, as they require no further surface metallization. However, they intrinsically suffer from a relatively large RF loss due to surface roughness of the printed metal. The other way is stacking nonconductive materials followed by surface metallization, such as stereolithography apparatus (SLA) that features a high printing resolution and a small surface roughness of the printed resin. SLA printing of waveguide devices starts from ultraviolet-laser curing of photosensitive resins layer by layer for defining the shape. Then, the printed resin structures are surface-metallized with highly conductive metals such as copper, silver, and gold. Several SLA-printed exponents to be highlighted in open literature are waveguides and their derivatives [5]–[9], cavity and waveguide filters [10]–[16], and horn antennas and arrays [5], [17]–[19] operating at frequencies from ultra-high-frequency (UHF) to submillimeter wave band. Due to the use of low-density resins, a dramatic reduction in the weight and redundant structural material of these devices is achieved without compromising any of their RF performance.

A ''split-block'' concept, i.e., splitting the electronic model into multiple parts for SLA printing and surface metallization, is adopted in pioneering implementations of these devices such as the *Ku*-band and UHF connectorized cavity filters in [10] and [11], the *X*-band waveguide filter in [12], and the *Ka*-band orthomode transducer in [20]. The purpose of splitting is to facilitate the electroplating process by fully exposing internal surface of the resin structure. However, the large RF loss induced by misalignment and stress-induced resin deformation makes this approach unsuitable for applications at even higher frequencies.

An effective pathway to metallize the internal resin surface by electroplating without splitting the structure is opening holes and slots on the sidewall of the cavity [13]–[15], [18], [21]. With these openings, the static electric field can be generated inside the cavity during electroplating process, and furthermore an active interaction of plating solution inside and outside the cavity is possible. It should be noticed that for non-radiation purpose as in [13]–[15] and [21] these openings are properly designed so as not to cut the internal surface current. Therefore, RF performance of these devices is not much influenced. Other supplementary measures such as auxiliary anodes can be used to assist the electroplating, but may at expense of extra cost, time, and operational inconvenience. This method can be also helpful to surface metallization techniques other than electroplating. However, it can be much less effective for devices at even higher frequencies, because extremely small holes cannot be well printed out, whereas enlarging them may result in unwanted RF-performance degradation. Therefore, reliable surface metallization process for such monolithically SLA-printed enclosed architectures needs to be explored.

Several related studies focusing metal plating of the SLA-printed devices have been presented in [5], [6], [8]–[10], and [16]. It should be mentioned that the state-of-the-art resin-based electroless metal plating technique as reported in [5] and [6] to date comes from a proprietary process that is developed on a proprietary polymer. No detail on the plating process is available. The plating recipes developed by Shen *et al.* [8], [9] are optimized on acrylate-based photopolymer substrates, claiming the lowest insertion loss (IL) of 0.16 dB/in to date for the 3-D printed *W*-band waveguides. The other plating techniques in [10] and [16] through either metal sputtering or spray-coating conductive ink, followed by electroplating to thicken the metal sheet, are not suitable for monolithically printed enclosed structures.

This paper presents an alternative solution to address the aforementioned technical issues. A comprehensive study on the RF design, 3-D printing, and surface metallization of a new family of millimeter-wave waveguide BPFs is reported. These filters are based on compact hemispherical resonators. In addition to a high unloaded quality factor (Q_u), the proposed hemispherical resonator benefits a volume only half of a spherical resonator [12] at a same resonant frequency, contributing to a size miniaturization and a high integration of the constituent devices. More significantly, it is much less degenerate than the latter due to its geometrical asymmetry, which contributes to improved out-of-band rejections for the constituent BPFs as compared to the counterpart in [12]. In this work, second- and fourth-order hemispherical resonator BPFs with various compact coupling configurations are designed at *X* and *Ka* bands, where four *Ka*-band filter prototypes are fabricated as proof of concept. Additionally to be highlighted in this paper is a proprietary recipe of the electroless nickel/copper/silver plating process that is developed on a series of commercially available resins. The proposed recipe can be further optimized for

more universal applications in metallizing SLA-printed structures.

The content of this paper is organized as follows. The theoretical foundation of the proposed hemispherical resonator is presented in Section II, where the electromagnetic (EM) field distribution of the resonant modes will be analyzed. The RF design of the hemispherical-resonator-based BPFs with several novel geometrical configurations is described in Section III. The SLA printing and surface metallization processes are discussed in Section IV. The RF-measured responses of various proof-of-concept filter prototypes are summarized in Section V. Finally, characterization of surface morphology for the SLA-printed samples is included in Section VI.

II. HEMISPHERICAL RESONATORS

The geometry of a hemispherical cavity is symmetrically half of a spherical cavity, which indicates a similarity in their resonant modes and the corresponding EM field distribution. The EM field components of resonant modes in a spherical cavity can be derived by solving spherical Bessel functions in spherical coordinates [22], and the solutions have been summarized in [12]. Due to the geometrical symmetry, a spherical cavity is highly degenerate and its dominant TM_{101} mode and some other higher order modes have three orthogonal directions of polarization. The TM_{101} mode's EM field in the one direction is illustrated in Fig. 1. The field distribution was obtained using eigenmode solver in Computer Simulation Technology (CST) Studio Suite [23]. As can be seen, the EM field is symmetrical to the center X–Y plane. This center plane can be equivalent to an electric wall. Therefore, the dominant mode of a hemispherical cavity is also TM_{101} mode, and has a same EM field distribution to that of a spherical cavity in the region of $z > 0$, as is illustrated in Fig. 2. Its magnetic field component can be mathematically expressed as

$$H_{\varphi,\mathrm{TM101}} = \frac{A}{\sqrt{r}} J_{3/2}(kr)\sin\theta, \quad 0 \le \theta \le \frac{\pi}{2}, \tag{1}$$

where A and k are constants determined by the root of the eigenvalue equation, r is a variable representing the radius, $J_{3/2}(kr)$ is a spherical Bessel function expressed as [22]

$$J_{3/2}(kr) = \sqrt{\frac{2}{\pi kr}}\left(\frac{\sin kr}{kr} - \cos kr\right). \tag{2}$$

For the region of $z > 0$ in a spherical coordinate, the angle θ is defined in the range of 0–90°. Therefore, the magnetic field intensity of the TM_{101} mode reaches the maximum as $\theta = 90°$, whereas equals to zero as $\theta = 0°$, which can be intuitively seen in Fig. 2. In addition, the field components are determined by the radius variable r. This means that for a same radius, a hemispherical cavity has an identical resonant frequency of the dominant TM_{101} mode to that of a spherical one. This resonant frequency can be derived as

$$f_{\mathrm{TM101}} = \frac{\omega_{\mathrm{TM101}}}{2\pi} = \frac{y_{11}}{2\pi r\sqrt{\mu\varepsilon}} = \frac{2.744}{2\pi r\sqrt{\mu\varepsilon}}, \tag{3}$$

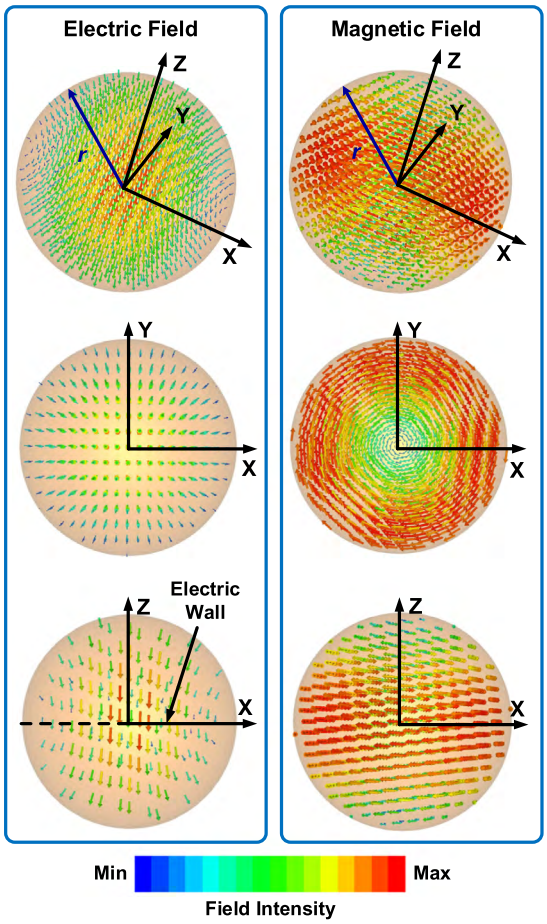

FIGURE 1. EM field distribution of the dominant TM_{101} mode in one of three orthogonal directions of polarization in a spherical cavity.

where ω_{TM101} is the corresponding angular frequency and the root y_{11} of the eigenvalue equation equals to 2.744 for TM_{101} mode [22]. The parameters μ and ε are permeability and permittivity of the dielectric filled in the cavity. This frequency for free space can be calculated as

$$f_{\mathrm{TM101}} \approx \frac{1.3102 \times 10^{11}}{r} \quad (\mathrm{Hz}), \tag{4}$$

with the unit of r in millimeter. For example, at an eigenmode resonant frequency of 10 GHz, the calculated radius of the cavity is around 13.1 mm. This is verified by performing EM simulation in CST, and the corresponding results are plotted in Fig. 3(a). Excellent agreement between the EM-simulated and the calculated eigenmode frequencies is obtained. The numerical calculation was performed in MATLAB [24].

The mathematical derivation for Q_u of the dominant TM_{101} mode in a metal-shielded and dielectric-filled hemispherical resonator is reported for the first time in this paper. The derivation begins with calculation of the Q_u for a spherical resonator. Generally, the Q_u of a metal-shielded vacuum sphere can be defined as [25]

$$Q_u = \omega\frac{W}{P_c}, \tag{5}$$

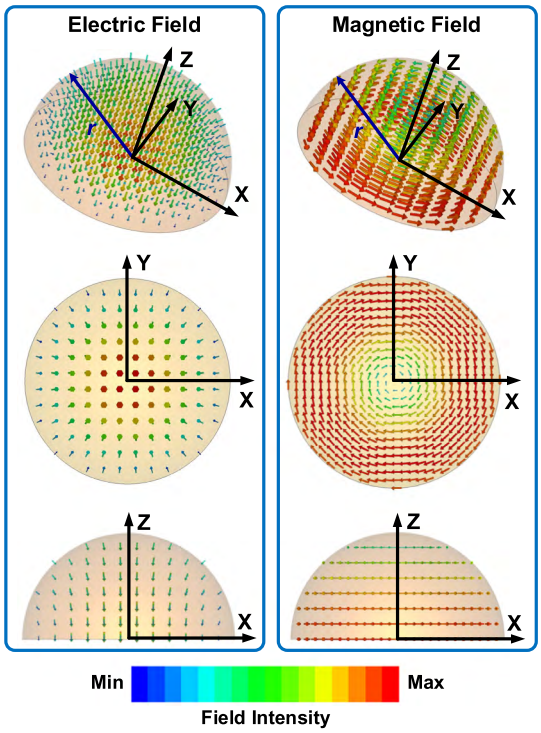

FIGURE 2. EM field distribution of the dominant TM_{101} mode in a hemispherical cavity. Only one direction of polarization is existent.

where W and P_c are the stored energy and the conductive power loss in the sphere, respectively. The stored energy W for the TM_{101} mode can be determined using the following integral

$$W = \frac{1}{2}\mu_0 \int_0^{2\pi}\int_0^{\pi}\int_0^{r} (\mathbf{H}\cdot\mathbf{H}^*) r^2 \sin\theta \mathrm{d}r\mathrm{d}\theta\mathrm{d}\varphi, \quad (6)$$

where $\mu_0 = 4\pi \times 10^{-7}$ H/m is the vacuum permeability. For the TM_{101} mode, since

$$\begin{cases} H_r = 0 \\ H_\theta = 0 \\ H_\varphi = \dfrac{A}{\sqrt{r}} J_{3/2}(kr)\sin\theta, \end{cases} \quad (7)$$

the equation (6) yields

$$W = \frac{4}{3}\mu_0 k A^2 r^3 \left[j_1^2(kr) - j_0(kr)\, j_2(kr)\right], \quad (8)$$

where

$$\begin{cases} j_0(kr) = \sqrt{\dfrac{\pi}{2kr}} J_{1/2}(kr) \\ j_1(kr) = \sqrt{\dfrac{\pi}{2kr}} J_{3/2}(kr) \\ j_2(kr) = \sqrt{\dfrac{\pi}{2kr}} J_{5/2}(kr). \end{cases} \quad (9)$$

The conductive power loss P_c is induced by the finite electrical conductivity σ of the metal shell from the spherical surface, and can be calculated by the following integral

$$P_c = \frac{1}{2}R_s \iint_{S_s} |\mathbf{H}|^2 \mathrm{d}S = \frac{8}{3}R_s k A^2 r^2 j_1^2(kr), \quad (10)$$

where R_s and d are the sheet resistance of the metal shell and the skin depth, respectively. Therefore, the Q_u for the spherical resonator is obtained using (5), (8), and (10) as

$$Q_u = \frac{\mu_0 \omega r \left[j_1^2(kr) - j_0(kr)\, j_2(kr)\right]}{2R_s j_1^2(kr)}. \quad (11)$$

In case of a hemispherical resonator, the corresponding stored energy W' in the hemisphere and the conductive power loss P_h from the hemispherical surface are half of those in a spherical resonator, and they are given as

$$W' = \frac{2}{3}\mu_0 k A^2 r^3 \left[j_1^2(kr) - j_0(kr)\, j_2(kr)\right] \quad (12)$$

and

$$P_h = \frac{4}{3}R_s k A^2 r^2 j_1^2(kr). \quad (13)$$

The equations (12) and (13) can also be derived from the equations (6) and (10) by simply replacing the integral upper limit of π with $\pi/2$ for the angle θ.

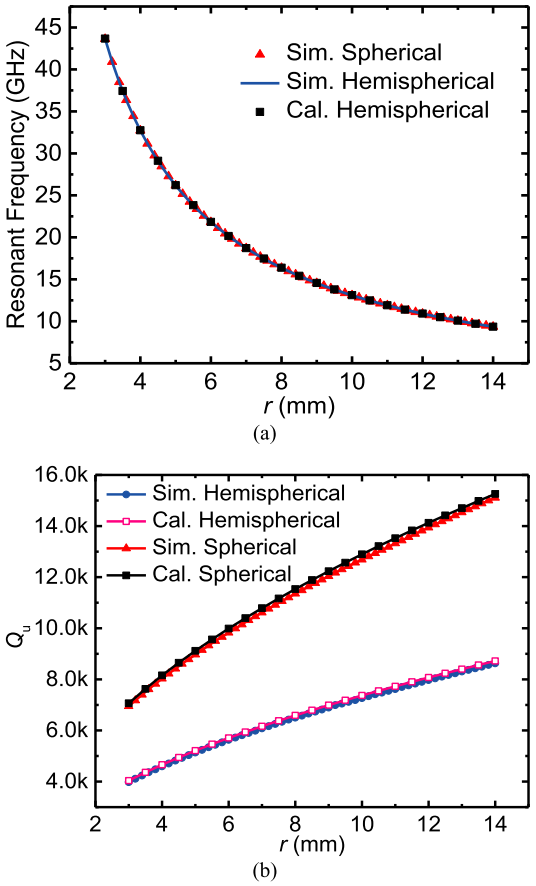

FIGURE 3. Eigenmode-simulated results of a single resonator. (a) Resonant frequencies of the dominant TM_{101} mode versus the radius. (b) Q_us versus the radius. The copper electrical conductivity $\sigma = 5.96 \times 10^7$ S/m was used.

The conductive power loss component P_r from the bottom round sheet of a hemispherical cavity is determined by the surface current density $\mathbf{J}_s$ that can be calculated as

$$\mathbf{J}_s = \mathbf{n} \times \mathbf{H} = \mathbf{n} \times \boldsymbol{\varphi} H_\varphi \big|_{\theta=90^\circ} = \mathbf{r} \frac{A}{\sqrt{r}} J_{3/2}(kr), \quad (14)$$

where $\mathbf{n}$ is the unit normal vector of the bottom surface. Hence, P_r can be calculated as

$$P_r = \frac{1}{2} R_s \iint_{S_r} |\mathbf{J}_s|^2 \, dS = \pi R_s A^2 \int_0^r J_{3/2}^2(kr) dr \quad (15)$$

The numerical integral in the equation (15) was calculated in MATLAB, and by integrating (5), (12), (13), and (15), the Q_u for the TM_{101} mode in a hemispherical resonator was obtained. The MATLAB-calculated Q_u values are plotted in Fig. 3(b) in comparison with the eigenmode-simulated ones, showing excellent agreement that proves correctness of the aforementioned derivation. The electrical conductivity $\sigma = 5.96 \times 10^7$ S/m for copper was used in the calculation and simulation. A comparison in critical aspects for several types of cavity resonators at 10 GHz is summarized in Table 1. The results in Fig. 3(b) and Table 1 indicate an intrinsically high quality factor of a hemispherical resonator, e.g., 8336 at 10 GHz ($r = 13.1$ mm) and 4644 at 32 GHz ($r = 4.1$ mm). Despite the fact that these Q_us are around 42% smaller than those of a spherical resonator due to the volume reduction, they are still sufficiently high for engineering applications at these frequency bands.

TABLE 1. Comparison of four types of cavity resonators at 10 GHz.

Resonators	Q_u	Dimensions (mm)	Volumes (mm^3)	First Higher Order Mode Frequencies (GHz)
Hemispherical	8336	13.1 (Radius)	4708.4	14.1 (TM_{201})
Spherical	14450	13.1 (Radius)	9416.8	14.1 (TM_{201})
Rectangular	7957	22.86 × 10.16 × 19.9	4621.9	15.1 (TE_{201})
Cylindrical	11200	10 (Radius) × 31.5	9896.0	13 (TE_{112})

TABLE 2. Mode frequencies (GHz) of two types of cavity resonators.

Resonators	TM_{101}			TM_{201}			TM_{211}	TM_{221}	TE_{101}		
	1	2	3	1	2	3	1	1	1	2	3
Hemispherical	10.0	—	—	14.1	14.1	—	—	—	16.37	16.37	—
Spherical	10.0	10.0	10.0	14.1	14.1	14.1	14.1	14.1	16.37	16.37	16.37

More importantly, a hemispherical resonator contributes to a reduction in the number of degenerate modes as compared to a spherical one. A summary of several higher order modes of interest and their resonant frequencies for these two types of resonators is included in Table 2. The numbers named below each mode indicate the degenerate modes of different orientations of polarization. In a hemispherical resonator, only one orientation of polarization exists for the TM_{101} mode, and two orientations of polarization exist for the TM_{201} and TE_{101} modes. The TM_{211} and TM_{221} modes are not existent. Therefore, the hemispherical resonator is much less degenerate. This indicates a potentiality of acquiring better out-of-band rejections with size-compact geometries for the hemispherical resonator BPFs than the spherical-resonator-based counterparts of the same orders. In the next Section, several designs of millimeter-wave waveguide BPFs based on hemispherical resonators will be presented. Compact inter-resonator coupling structures with enhancement in the filters' out-of-band rejections will be discussed.

III. DESIGN OF HEMISPHERICAL RESONATOR BPFS

A. X- AND KA-BAND SECOND-ORDER BPFS

The first devised inter-resonator coupling structure with a good geometrical compactness is illustrated in Fig. 4(a). It is composed of a pair of back-to-back hemispherical resonators that are aligned at their centerline and are connected by a fan slot in between. The fan slot has a thickness of t, as labeled in Fig. 4(a), which separates these two hemispheres to each other. The inter-resonator coupling is achieved mainly by the coupled magnetic field through the fan slot, and its strength can be controlled either by the length r_{iris} or the angle θ of the fan, as labeled in Fig. 4(b). The denormalized inter-resonator coupling coefficient k_{12} can be extracted as functions of r_{iris} and θ, and they are plotted in Fig. 4(c) and 4(d), respectively. The extraction of k_{12} was performed in EM simulation using the process outlined in [26] for magnetically coupled and synchronously tuned resonators. The k_{12} can be expressed as $k_{12} = (f_{p2}^2 - f_{p1}^2)/(f_{p2}^2 + f_{p1}^2)$, where f_{p2} and f_{p1} represent the lowest two eigenmode resonant frequencies for the two coupled resonators in Fig. 4(a). Figs. 4(c) and 4(d) show that k_{12} increases as either r_{iris} or θ increases, which can be understood straightforwardly. The fan slot is radially placed in the ring region with the strongest magnetic field so as to acquire a relatively large coupling strength.

Using this inter-resonator coupling structure, a second-order BPF with a Chebyshev transfer function was designed as the first example. The filter was designed at a center frequency (f_0) of 10 GHz with a 1% fractional bandwidth (FBW) and a passband return loss (RL) of 20 dB. Its corresponding non-zero denormalized coupling coefficients are $M_{S1} = M_{2L} = 0.0122$ and $M_{12} = 0.0166$. Fig. 5 shows an overall air-box simulation model of the second-order BPF. The filter is fed by standard rectangular waveguides, and its external coupling strength is controlled by the width a_1 and the height b_1 of a rectangular window at the end of the feeding waveguide. The external quality factor (Q_e) associated with the external coupling coefficients M_{S1} and M_{2L} can be calculated from the group delay of the S_{11} parameter for a singly loaded hemispherical resonator [26]. The extracted Q_e values in relation to a_1 are plotted in Fig. 6.

Using the filter design methodology in [26], the desired X-band bandpass filtering response was obtained by

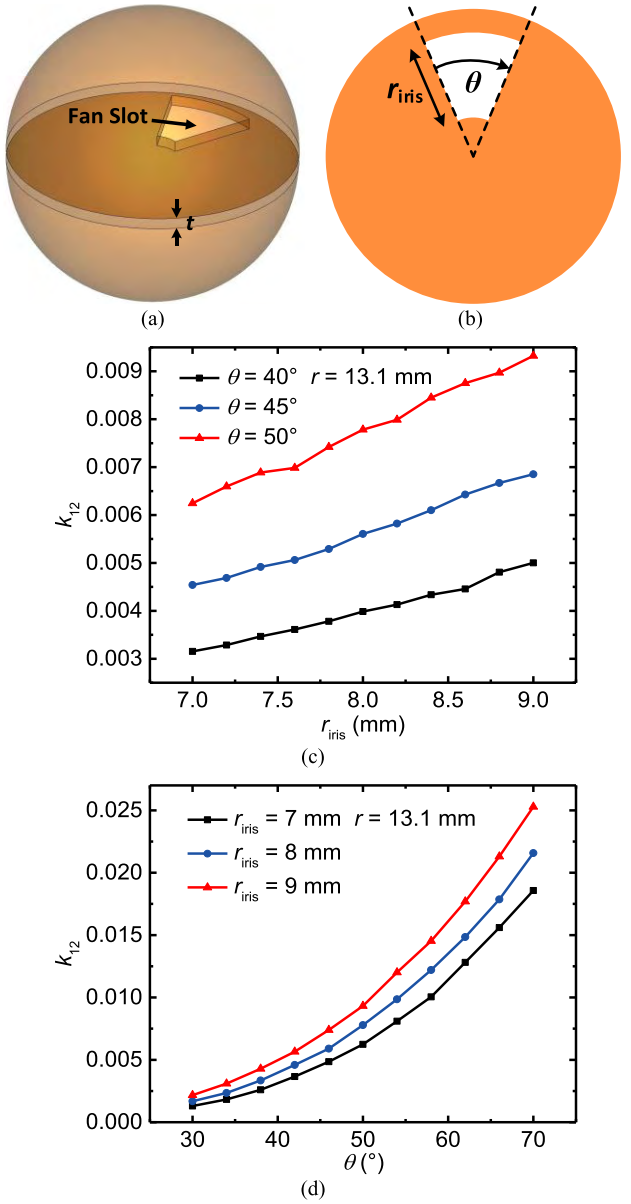

FIGURE 4. The coupling iris and extracted coupling coefficients k_{12} between a pair of back-to-back hemispherical resonators. (a) An air-box simulation model of the coupled resonators. (b) A structural illustration of the fan slot. (c) k_{12} versus r_{iris}. (d) k_{12} versus θ. An iris thickness $t = 1$ mm was used.

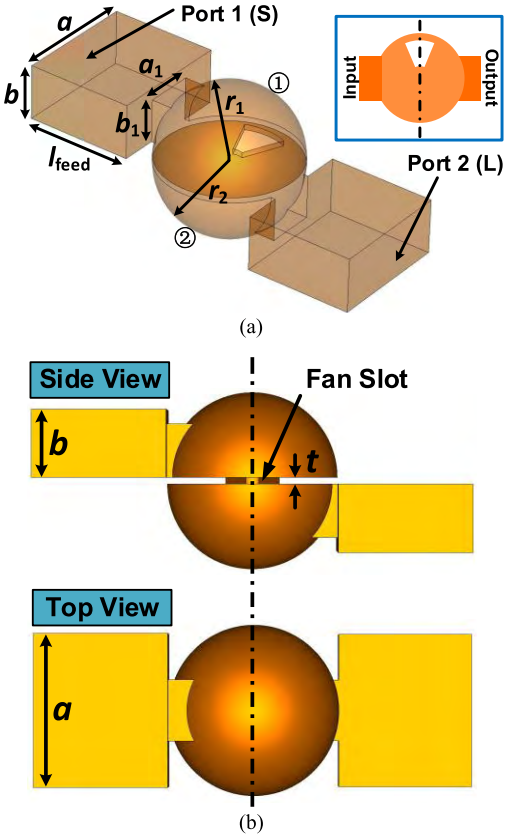

FIGURE 5. An air-box simulation model of the designed second-order BPF based on hemispherical resonators. (a) The 3-D view, where *a*, *b*, and l_{feed} denote width, height, and length of the feeding waveguide; S: source; L: load. (b) The side and top views.

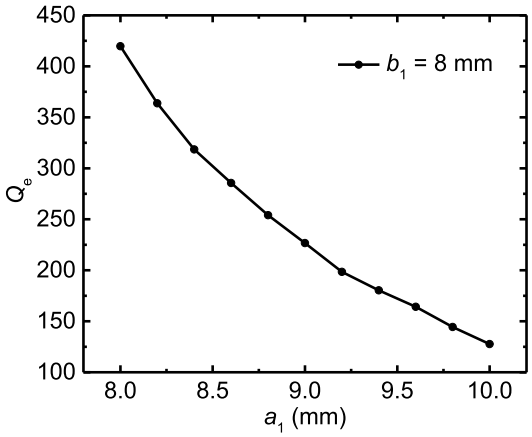

FIGURE 6. The extracted Q_e from EM simulation versus a_1.

performing EM simulation in CST. The EM-simulated passband performance is plotted in Fig. 7(a). A parasitic transmission zero (TZ) is found around 12.1 GHz [Fig. 7(b)] due to cancellation of out-of-phase signals propagating along two different paths in the hemispherical resonator. The magnetic field distribution inside the filter at the frequencies of the passband center and the TZ is illustrated in Fig. 8. At 10 GHz, a relatively strong TM_{101}-mode magnetic field is generated inside the hemispherical resonators and can be coupled to the output. On the other hand, at the TZ frequency, a large portion of the field energy is reflected to the input and a very weak magnetic field is generated inside the first hemispherical resonator. Due to the phase-difference-induced signal cancellation at the fan slot, little field energy is coupled to the secondary hemispherical resonator and the output. The frequency of the TZ is dependent on the phase difference between the two signal propagation paths, and is controlled by the orientation of the fan slot. This is verified by a group of EM-simulated

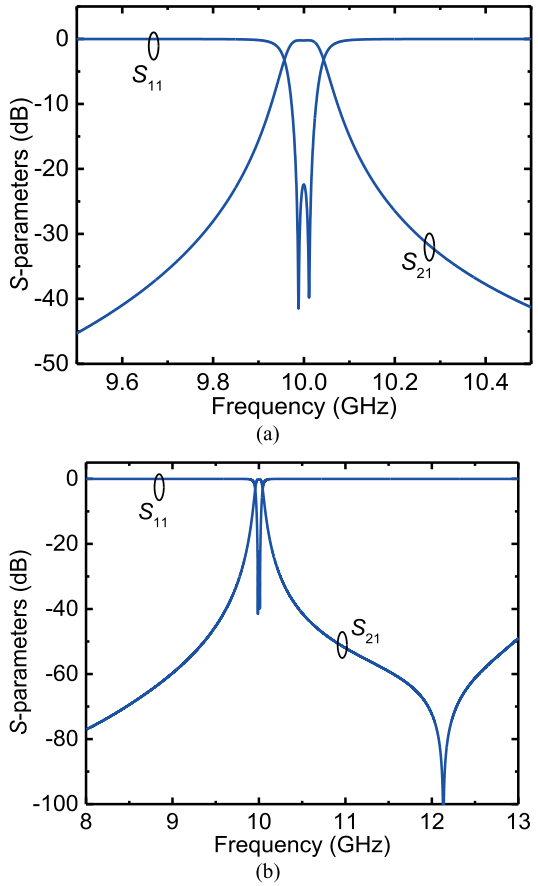

FIGURE 7. EM-simulated frequency response of the designed *X*-band 1%-FBW second-order hemispherical resonator BPF. (a) The passband detail. (b) The wideband performance.

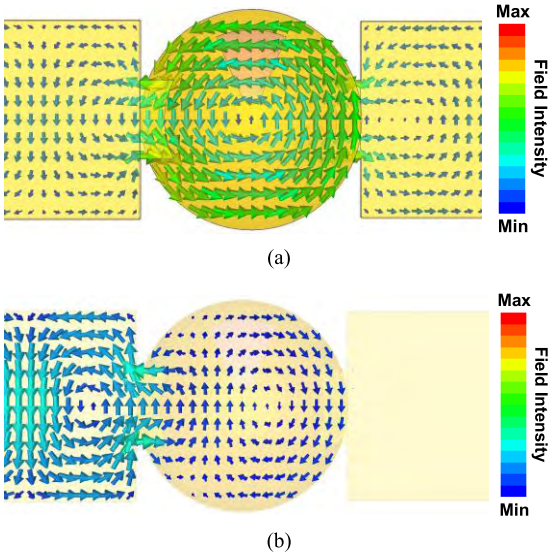

FIGURE 8. Magnetic field distribution in the designed *X*-band second-order BPF. (a) At the f_0 of 10 GHz. (b) At the TZ frequency of 12.144 GHz.

transmission coefficients as depicted in Fig. 9 with various values of the orientation angle φ. It is found that the two groups of S_{21} parameter for $\varphi = 30°$ and $\varphi = 150°$ as well

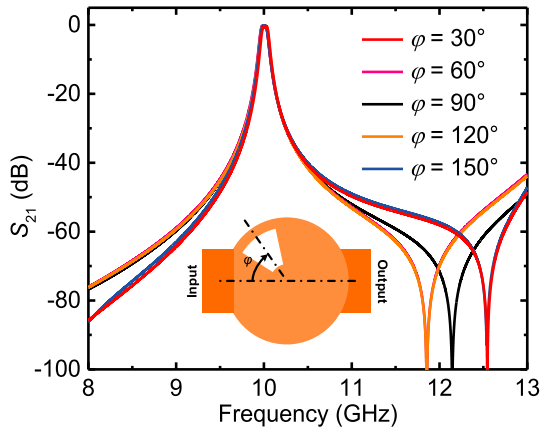

FIGURE 9. EM-simulated S_{21} parameter of the *X*-band 1%-FBW second-order hemispherical resonator BPF under different orientation angles for the fan slot.

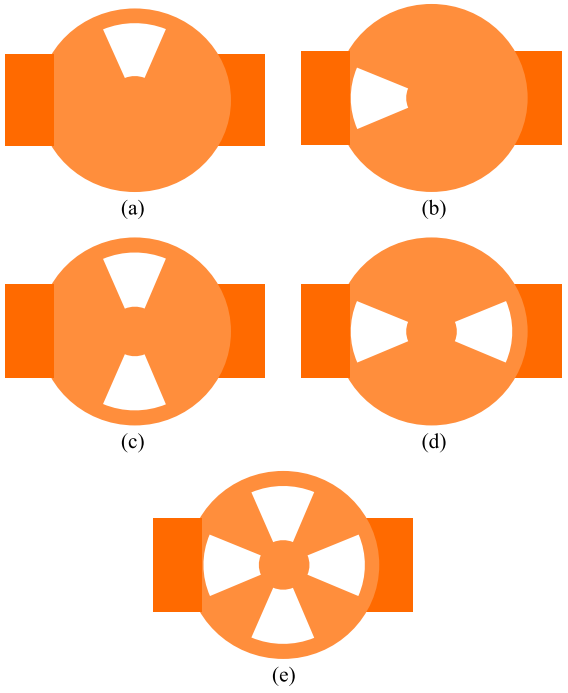

FIGURE 10. Structural comparison of various fan slot coupling irises. (a). The single-fan iris ($\varphi = 90°$). (b) The single-fan iris ($\varphi = 0°$). (c) The dual-fan iris ($\varphi = 90°$). (d) The dual-fan iris ($\varphi = 0°$). (e) The orthogonal quad-fan iris.

as $\varphi = 60°$ and $\varphi = 120°$ overlap because of the reciprocity and structural symmetry of the filters. In this design, the fan slot is placed perpendicular [$\varphi = 90°$, see Fig. 5(a) inset and Fig. 10(a)] to the input-to-output direction in order to achieve the best out-of-band rejection. Several other coupling iris configurations with more numbers of fan slots and different slot orientations can be designed, as illustrated in Figs. 10(b)–10(e). The EM-simulated frequency responses for the 1%-FBW second-order BPFs employing these irises are plotted in Fig. 11. Note that all the filter designs involved in Fig. 11 are capable of realizing an ideal passband reflection

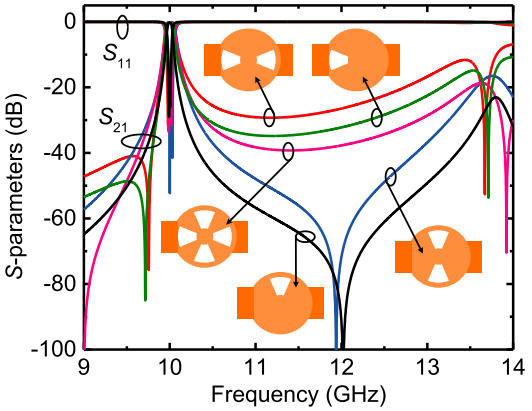

FIGURE 11. EM-simulated frequency responses of the *X*-band 1%-FBW second-order hemispherical resonator BPFs using different coupling iris configurations.

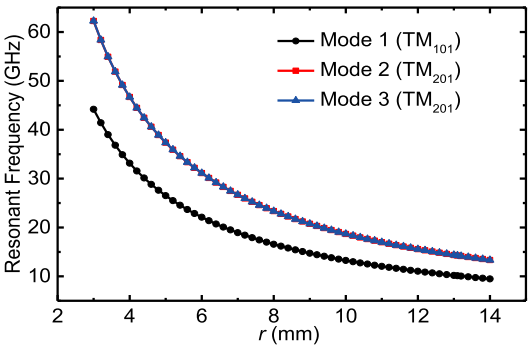

FIGURE 12. Eigenmode-simulated resonant frequencies of the TM_{101} (reference) and TM_{201} modes in a hemispherical resonator as functions of the radius.

coefficient, i.e., $S_{11} < -20$ dB, and the physical dimensions of the corresponding fan slots are slightly different. As can be seen, the filter using the $\varphi = 90°$ single-fan iris achieves the best high-side out-of-band rejection, whereas the one using the $\varphi = 0°$ dual-fan iris [Fig. 10(d)] has the worst high-side out-of-band rejection. This is attributed to properly controlling the amount of inter-resonator coupling for the first higher order mode, i.e., TM_{201} mode (see Tables 1 and 2). The TM_{201} mode is degenerate and has two orthogonal directions of polarization. These two degenerate TM_{201} modes have a same resonant frequency, which is verified by the eigenmode-simulated results plotted in Fig. 12. The magnetic field distribution in these two directions of polarization is graphically presented in Fig. 13. With a single-fan iris configuration, a smallest coupling from the TM_{201}-mode magnetic field can be achieved under circumstance of $\varphi = \pm 90°$. This is because in this scenario the fan slot is located in an area with a relatively weak TM_{201}-mode magnetic field. On the other hand, a strongest coupling from the TM_{201}-mode magnetic field can be realized in case of either $\varphi = 0°$ or 180°. Furthermore, the coupling from the TM_{201}-mode magnetic field will be strengthened as the number of fan slots increases. Also noteworthy is the disappearance of the parasitic TZ around 12 GHz for iris configurations containing either

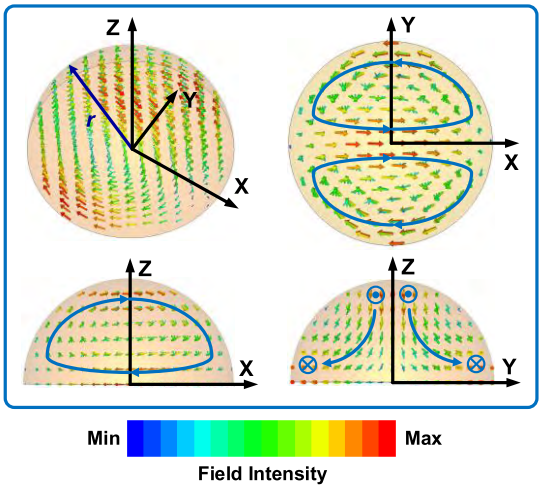

FIGURE 13. Magnetic field distribution of the degenerate TM_{201} modes in a hemispherical resonator. (a) In the first polarization direction. (b) In the second polarization direction.

$\varphi = 0°$ or 180° fan slots. In such cases, the out-of-phase cancellation of signal is not practical due to the symmetry.

To conclude, the aforementioned description has well interpreted that the filters with iris configurations in Fig. 10(b)–10(e) suffer from worse high-side out-of-band rejections, and thus the design in Fig. 10(a) is finalized for the second-order BPF. The optimized critical dimensions for the *X*-band filter's air-box simulation model are $a = 22.86$ mm, $b = 10.16$ mm, $l_{\text{feed}} = 20$ mm, $a_1 = 9.25$ mm, $b_1 = 8$ mm, $r_{\text{iris}} = 8$ mm, $\theta = 46°$, $r_1 = r_2 = 12.78$ mm, and $t = 1$ mm. Fig. 14 includes a structural illustration for the filter's fabrication model. The model can be hardly implemented as a single part by using a conventional CNC milling technique. However, its monolithic actualization by using 3-D printing is possible. For purpose of a fast and low-cost experimental validation, the devised filter was scaled to *K*a band with the following RF specifications—f_0: 32 GHz, FBW: 1%, and RL: 20 dB (Filter A). The corresponding scaled dimensions are $a = 7.112$ mm, $b = 3.556$ mm, $l_{\text{feed}} = 10$ mm,

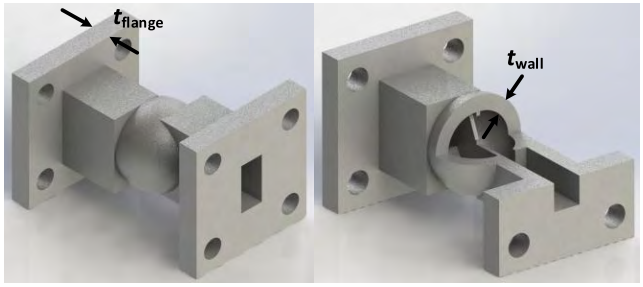

FIGURE 14. A fabrication model of the *Ka*-band second-order hemispherical resonator BPF (Filter A). (a) The complete drawing. (b) The profile view.

$a_1 = 3.08$ mm, $b_1 = 2$ mm, $r_{iris} = 3$ mm, $\theta = 48°$, $r_1 = r_2 = 3.97$ mm, and $t = 0.5$ mm. Note that in addition to a frequency mapping, the size scaling has no other influence on the filter's transfer function such as the TZ and the out-of-band rejection. Therefore, practical RF performance of the *X*-band filter can be equivalently characterized by evaluating that of the *Ka*-band prototype. Standard WR28 waveguide flanges are used for the input and output of the *Ka*-band prototype. The thicknesses of the cavity shells t_{wall} and the flanges t_{flange} (labeled in Fig. 14) are designed to be 2 and 3 mm, respectively, in a compromise of mechanical strength and fabrication cost. The filter's manufacturing will be detailed in Section IV.

B. X- AND KA-BAND FOURTH-ORDER BPFS

An extensive research on the hemispherical-resonator-based RF design was carried out focusing higher order BPFs with compact and interesting inter-resonator coupling geometries. In this part, two highly integrated fourth-order hemispherical resonator BPFs are exemplified. Their air-box simulation models are graphically presented in Figs. 15 and 16. For each

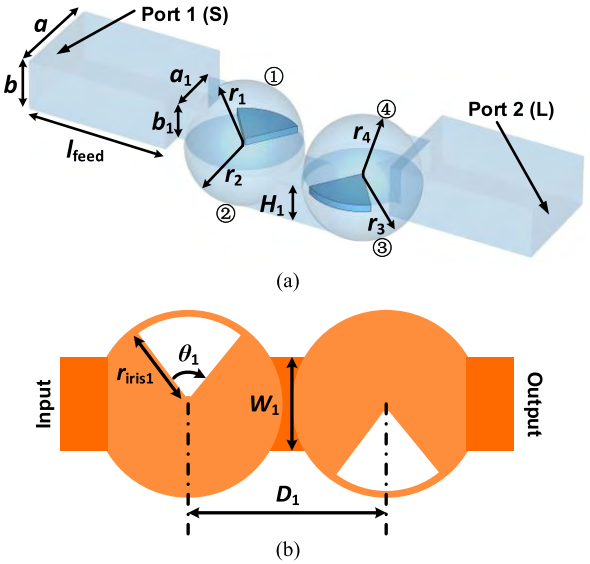

FIGURE 15. A structural illustration of the fourth-order hemispherical resonator BPF (Filter B) with one parasitic TZ. (a) The air-box simulation model. (b) The coupling iris configuration.

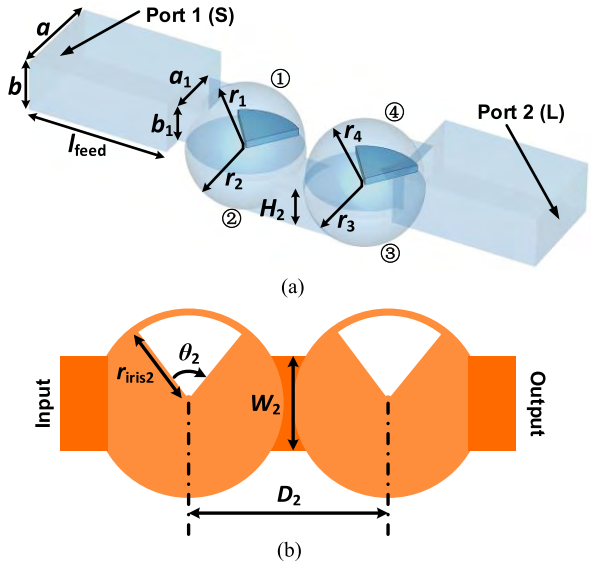

FIGURE 16. A structural illustration of the fourth-order hemispherical resonator BPF (Filter C) without the parasitic TZ. (a) The air-box simulation model. (b) The coupling iris configuration.

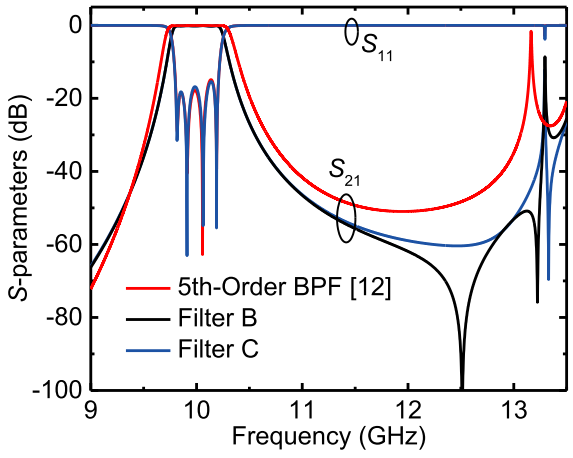

FIGURE 17. EM-simulated frequency responses of the *X*-band 5%-FBW fourth-order hemispherical BPFs with (Filter B) and without (Filter C) the parasitic TZ.

filter, two pairs of back-to-back hemispherical resonators are utilized and are connected by a section of rectangular cavity between the second and the third resonators. The coupling strength between the resonators 2 and 3 can be controlled by the width and length of the cavity [labeled as W_1, W_2, D_1, and D_2 in Figs. 15(b) and 16(b)]. The two fan slots in Fig. 15 have orientation angles of $\varphi_1 = 90°$ and $\varphi_2 = -90°$ (Filter B), whereas the two slots in Fig. 16 have an identical angle of $\varphi_1 = \varphi_2 = 90°$ (Filter C). The phase difference induced by these two iris configurations results in different out-of-band transmission characteristics. This can be validated from the EM-simulated results of the two *X*-band fourth-order BPFs as plotted in Fig. 17. The two filters were designed at an f_0 of 10 GHz with a 5% FBW and a 20-dB passband RL. The corresponding non-zero denormalized coupling matrix

entries are $M_{S1} = M_{4L} = 0.0518$, $M_{12} = M_{34} = 0.0455$, and $M_{23} = 0.0350$. The Filter B exhibits a parasitic TZ at around 12.5 GHz that is not existent for the Filter C. Furthermore, the designed fourth-order BPFs perform even better out-of-band rejections than that of the fifth-order spherical resonator BPF in [12].

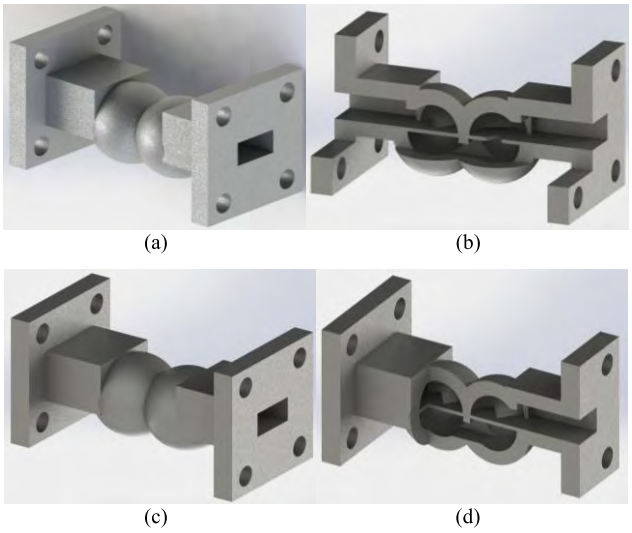

FIGURE 18. Fabrication models of the *Ka*-band fourth-order hemispherical resonator BPFs. (a) Filter B: the complete drawing. (b) Filter B: the profile view. (c) Filter C: the complete drawing. (d) Filter C: the profile view.

The two fourth-order filters were then scaled to *Ka* band at an f_0 of 32 GHz and their fabrication models are illustrated in Fig. 18. The thicknesses of the cavity shells and the flanges are the same to those of the Filter A. Critical dimensions of the Filters B and C are summarized in Table 3.

TABLE 3. Critical dimensions of the filters B and C at Ka Band (Unit: mm).

Filter	a	b	l_{feed}	a_1	b_1	r_1	r_2
B	7.112	3.556	10	3.972	2.5	3.763	3.86
r_3	r_4	θ_1	r_{iris1}	D_1	W_1	H_1	t
3.86	3.763	72.71	3.683	8.5	3.787	2.5	0.5
Filter	a	b	l_{feed}	a_1	b_1	r_1	r_2
C	7.112	3.556	10	3.972	2.5	3.763	3.86
r_3	r_4	θ_2	r_{iris2}	D_2	W_2	H_2	t
3.86	3.763	72.71	3.683	8.5	3.787	2.5	0.5

Presented in the last part of this Section is a fourth-order hemispherical resonator BPF with the other size-compact zigzag coupling geometry also demonstrating an improved out-of-band rejection. The designed inter-resonator and external coupling structures are different from all the aforementioned examples, and exhibit a superior capability of suppressing the TM_{201} mode. The filter's air-box simulation model and fabrication model are shown in Fig. 19. The four hemispherical resonators are placed in line to the input-to-output direction. Three circular slots and a pair of

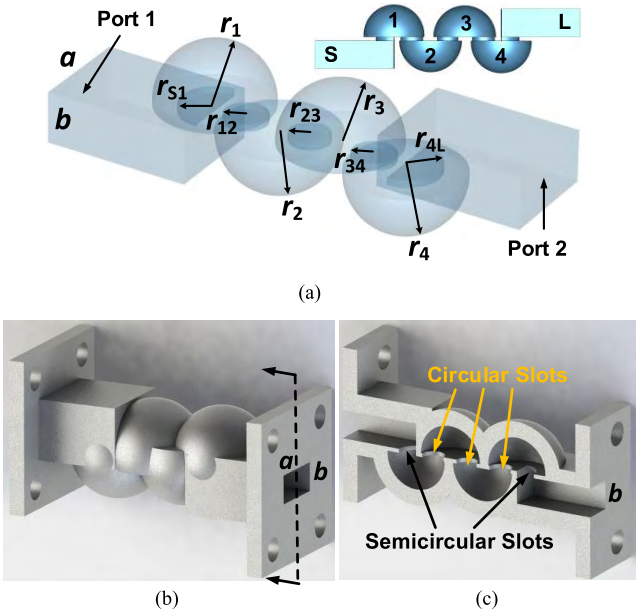

FIGURE 19. A structural illustration of the fourth-order hemispherical resonator BPF with a zigzag coupling configuration. (a) The air-box simulation model. (c) The complete drawing of the fabrication model. (d) The profile view of the fabrication model.

semicircular slots are used for the inter-resonator and the external couplings, respectively. The circular slots contribute to cancellation of out-of-phase magnetic field components of the TM_{201} mode (see the magnetic field distribution in Fig. 13). Therefore, the filter's out-of-band rejection can be significantly improved. This filter was first designed at *X* band with the following RF specifications—f_0: 10 GHz, FBW: 3%, and RL: 20 dB, and was then scaled to *Ka* band (Filter D) for fabrication. The EM-simulated result of the *X*-band filter is summarized in Fig. 20. It shows that the filter offers an over 50-dB rejection from 10.6 to 13.6 GHz that is over 25 dB higher than that for the dual-mode spherical resonator BPF proposed in [13]. This again exemplifies advantages of hemispherical resonators in offering much less numbers of higher order modes and flexible coupling structures for suppression of them. The optimized critical dimensions for the Filter D are $a = 7.112$ mm, $b = 3.556$ mm, $r_1 = r_4 = 3.893$ mm, $r_2 = r_3 = 4.02$ mm, $r_{12} = r_{34} = 1.448$ mm, $r_{23} = 1.357$ mm, and $r_{S1} = r_{4L} = 2.327$ mm.

IV. DEVICE FABRICATION

In this Section, the manufacturing process for the *Ka*-band BPF demonstrators will be expounded. The first part will describe the AM and the relevant post processes in this work. The second part will focus surface metallization of the structures by adopting a proprietary electroless plating technique.

A. SLA PRINTING PROCESS

A proprietary industrial-grade SLA 3-D printer (model No.SLA-300S) developed by the Shanghai New East China Institute of Optoelectronic Technology [27] was applied.

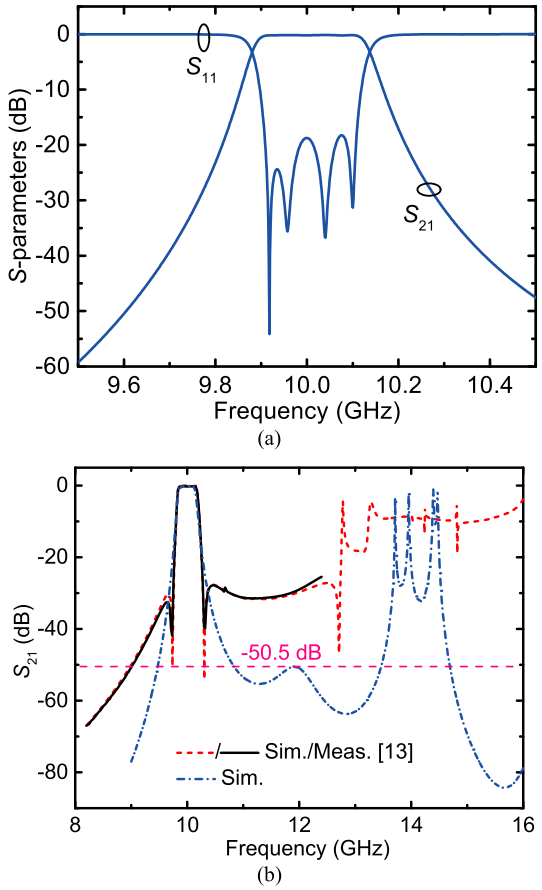

FIGURE 20. EM-simulated frequency responses of the *X*-band 3%-FBW fourth-order hemispherical resonator BPF with a zigzag coupling configuration. (a) The passband performance. (b) The wideband performance.

The SLA printer is capable of printing in a high horizontal (X–Y) resolution of 1 μm × 1 μm and an adjustable vertical resolution of 50, 70, and 100 μm. A commercially available ceramic-filled photosensitive resin Somos® PerForm [28] was utilized as the printing material. This type of resin is superior in a better mechanical strength and a much better thermal handling capability than ordinary SLA-compatible resins such as Accura Xtreme [29], Somos 14120, and Somos Imagine 8000 [28]. Microwave characterization for thermal handling capability of Somos PerForm resin has been reported in [15]. The experimented filter in [15] made from such resin was able to operate at a temperature of over 140 °C with a low temperature-dependent frequency shift rate. On the other hand, the ordinary resins are usually working at a suggested temperature of no more than 50 °C and may suffer from a larger thermal deformation.

Before the SLA printing, electronic models of the filters were properly placed in their positions to make sure that the stacked printing material could be self-supported and thus no resin support would be used inside the cavities. In this case, relatively smooth surface of the resin cavity could be realized. The SLA printing was carried out in a vertical printing resolution of 50 μm. The average cost of printing each filter was less than $50.

After the ultraviolet-laser curing process was complete, the models were chemically cleaned in acetone for 5 minutes and then dried with compressed air. This was in order to dissolve uncured resin on the surface of the models. The models were double cured in an ultraviolet oven (a total ultraviolet-light source power: 144 W) for 30 minutes. During this curing, the models were surrounded by eight 18-W ultraviolet light tubes so that each surface could be uniformly irradiated. The double curing process enhanced mechanical strength of the resin.

The cured models were then sandblasted using #800 white sand stone under a sandblasting air pressure of 40 psi to remove resin residuals on the both internal and external faces. This was followed by a manual polishing process for the external surface by using 400, 600, and 1000 grits, successively, with combination use of water, whereas the inner surface cannot be manually polished.

The SLA printing process ended with an optimized heat treatment to the resin. This heat treatment further improved mechanical robustness as well as thermal handling capability of the resin. In this process, the models were hard baked in an infrared oven at 160 °C for 2 hours, with a temperature ramp-up rate on average of 1.3°C per minute. The hard baking ended with a natural cooling to the room temperature. It should be noted that this heat treatment is particularly designed for the PerForm resin. Heat treatment to ordinary-resin-based models may cause destructive deformations and thus is not suggested.

B. SURFACE METALLIZATION PROCESS

Summarized below are a tailor-made recipe of the electroless plating employed in this work to surface-metallize the SLA-printed resin structures. The plating process was performed in a cleanroom-grade industrial workshop.

1) DECONTAMINATION

The recipe began with decontamination of the SLA-printed models in isopropanol and deionized (DI) water.

2) SURFACE ACTIVATION

The resin surface was activated first by using an argon RF-plasma radiation in order to physically break chemical bonds on the resin surface. The surface-irradiated models were then chemically etched in the coarsening agent prepared with potassium permanganate and potassium hydroxide solutions. The resin models after surface roughening were rinsed with DI water and dried with compressed nitrogen. Next, the models were immersed into palladium chloride colloid so that a thin layer of palladium-based catalyst could be deposited onto the resin.

3) BARREL ELETROLESS PLATING

The barrel electroless plating started with deposition of a seed layer of nickel. An alkaline electroless nickel plating solution

prepared with sodium hypophosphite, nickel chloride, and ammonium chloride was utilized. The nickel plating was performed in a circulating filtration system with a solution temperature of 30–40 °C and a solution pH of around 9. A 0.2–0.4-μm thick layer of nickel was plated with catalysis of the pre-deposited palladium-based compound.

The electroless copper plating was also performed in a circulating filtration system accompanied with air agitation. The plating solution was prepared with copper sulphate, sodium hydroxide, ethylenediaminetetraacetic acid, and formaldehyde, and was controlled at a reaction temperature of 55–60 °C and a pH of around 12. A 5-μm thick layer of copper was plated. The time of plating for Filters B and C was intentionally increased to make sure a sufficient thickness of the metal could be reached inside the cavities.

The surface metallization process ended with deposition of a 1-μm thick passivation layer of silver. The electroless plating of silver was a replacement reaction of copper using silver nitrate solution and a proper complexing agent. The silver-plated models were then immersed into a silver protective agent to form a passivation layer in a nanometer-scale thickness on the surface of silver. This layer could prevent the silver from oxidation. It should be mentioned that the passivation layer exhibited a small sheet resistance and had no significant influence on electrical conductivity of the plated metal layer. A thin layer of gold could be used alternatively for purpose of passivation, but it needed to be deposited on another seed layer of nickel. Finally, the metal-plated models were rinsed with DI water and dried with compressed nitrogen.

Note that the designed thickness of 5 μm for the plated copper/silver layer was considered in the electronic models of the filters. This was realized by performing a structural compensation through subtracting the thickness from the cavity shell. If the structural compensation was not carried out, the introduced dimensional tolerance would cause undesired frequency shift and degradation of passband performance, and this could be more serious for devices operating at *W* band or even higher frequencies [30].

Technical features of the utilized barrel electroless plating process are summarized as follows.

1. The surface activation of the resin using an argon RF-plasma radiation effectively enhanced adhesion of the plated metal layer onto the resin. However, the plasma activation might be less effective to the unexposed internal surface.

2. A low-temperature recipe of the electroless plating was selected so that thermal-stress-induced imperfection in the plated metal layer could be minimized. Neither blistering nor skip plating of the metal layer was observed in the experiment.

3. The models were kept rolling during the barrel plating, and thus an active interaction of the plating solution inside and outside the cavities could be realized. Concentration of the plating solution in different regions of the models could be controlled more uniformly, which effectively equalized the deposition rate of the metal layer. In this way, sidewall openings were not needed in this work.

4. The recipe of electroless plating was developed also with a good compatibility to ordinary resins Somos 14120 and Somos 8000, but may subject to a small adjustment of the involved chemical additives.

V. RF-PERFORMANCE MEASUREMENT

Photographs of the manufactured *Ka*-band second-order hemispherical resonator BPF (Filter A) are shown in Fig. 21. RF-performance measurement of the filter was conducted by using a Keysight microwave network analyzer N5247A PNA-X [31] with a standard waveguide short-open-load-thru calibration. The RF-measured result of the Filter A is plotted in Fig. 22. Excellent agreement between the EM-simulated and RF-measured results can be seen. The passband frequency shift is about 0.04% (13 MHz) towards higher frequencies, indicating a good control of thickness and uniformity of the deposited metal layer as a result of barrel electroless plating. The measured IL is about 0.56−0.7 dB at 31.95−32.13 GHz, and the measured passband RL is better than 17 dB. A small increase of about 0.23 dB in the passband IL is attributed to the degradation of the resonator's Q_u. The practical Q_u can be extracted from the S_{21} parameter of a weakly coupled resonator network [26], however, for the *Ka*-band demonstration, the required window size for a weak external coupling would be too small so that the internal surface could not be satisfactorily metallized. The evaluation of practical Q_u of a single hemispherical resonator will be further discussed in Section VI. Since the total thickness of the plated metal layer is over 10× the skin depth d of the copper ($d \approx 0.37$ μm for copper at 32 GHz), the radiation loss can be neglected and the major IL increment is caused by conductive loss of the plated metal layer as a result of surface roughness. First, the inner surface of the resin cavity is not perfectly smooth because it is comprised of steps of multiple stacked layers. This imperfection could be further reduced if an even higher printing resolution (e.g., 25 μm) were used, but at expense of an increased fabrication cost. Secondly, the electrical conductivity of the plated copper layer is smaller than the ideal value (5.96×10^7 S/m) used in the EM

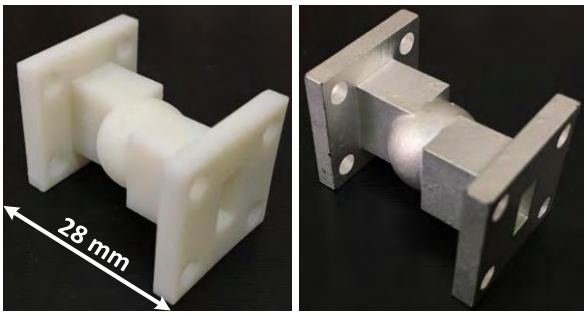

FIGURE 21. Photographs of the fabricated *Ka*-band second-order hemispherical resonator BPF (Filter A) before (left) and after (right) surface metallization.

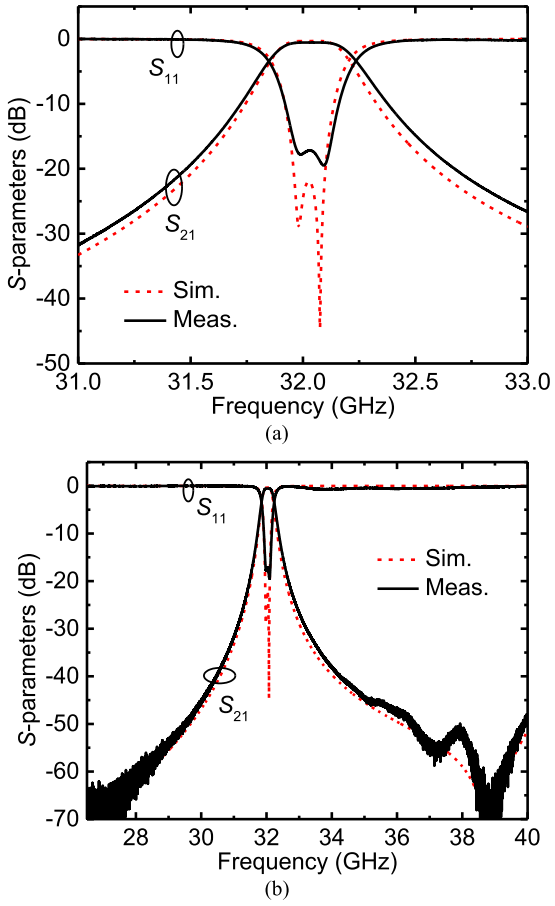

FIGURE 22. EM-simulated and RF-measured frequency responses of the *Ka*-band second-order hemispherical resonator BPF (Filter A). (a) The passband performance. (b) The *Ka*-band performance.

simulation. Unfortunately, these two aspects can be hardly quantified for the practical filter. Furthermore, the parasitic TZ is found around 39 GHz, and the measured high-side out-of-band rejection is over 40 dB from 34 to 40 GHz. With use of the low-density (∼1.61 g/cm^3 at 25 °C) and heat-resistant ceramic-filled resin, the engineered filter exhibits a light weight of 5.3 g and an attractive potentiality of operating at a much higher temperature than the counterparts made from ordinary resins.

Fig. 23 includes photographs of the fabricated *Ka*-band fourth-order hemispherical resonator BPFs (Filters B and C). The RF-measured frequency responses of the filters are plotted in Fig. 24, and agree reasonably with the EM-simulated ones. The measured passband frequency shifts are around 0.01% (5 MHz) and 0.47% (150 MHz) towards higher frequencies for the Filters B and C, respectively. The measured passband RLs are degraded to around 10 and 12 dB for the Filters B and C, and the corresponding passband ILs are 0.58–1 dB and 0.43–1 dB, respectively. Note that the Filter C's bandwidth is slightly enlarged, indicating the increased inter-resonator couplings as well as resonant frequencies as a result of the thicker-than-necessary metal layer.

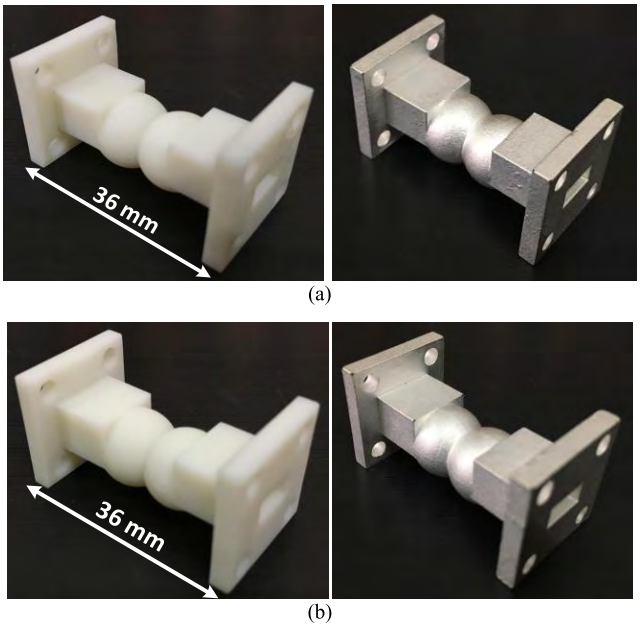

FIGURE 23. Photographs of the fabricated *Ka*-band fourth-order hemispherical resonator BPFs before (left) and after (right) surface metallization. (a) Filter B. (b) Filter C.

The measured out-of-band rejections are over 40 dB at 35−40 GHz for both filters.

The photographs and RF performance of the Filter D are graphically represented in Figs. 25 and 26. The filter's passband frequency shift is about 0.06%. The measured passband IL and RL are 0.43−0.9 dB and mostly better than 15 dB, respectively. The measured out-of-band rejection is over 40 dB at 34−40 GHz.

For these three fourth-order BPFs (Filters B, C, and D), the discrepancy in the passband RL should be noticed. In addition to the thickness tolerance in the plated metal layer, other two types of printing-material-related tolerances play important roles. First, the inevitable shape shrinkage due to phase change of the resin from liquid to solid can be a root cause of shape inaccuracy [32]. On the other hand, the gravity-induced creep of the resin during the laser curing process further leads to permanent deformations along the printing direction. Structural compensation can be useful to address the issue of shrinkage for simple shapes [33]. However, an accurate realization of the compensation is very difficult for complex geometries.

VI. CHARACTERIZATION OF SURFACE MORPHOLOGY

Surface morphology for the hemispherical cavity was characterized on two types of simplified geometries. They are flat circular discs and hemispherical shells. The surface quality of the feeding waveguide's internal wall and the fan-slot coupling iris for the demonstrated hemispherical resonator BPFs can be equivalently represented by quantifying the surface profile and roughness of the disc. Similarly, the surface quality of the internal hemispherical wall

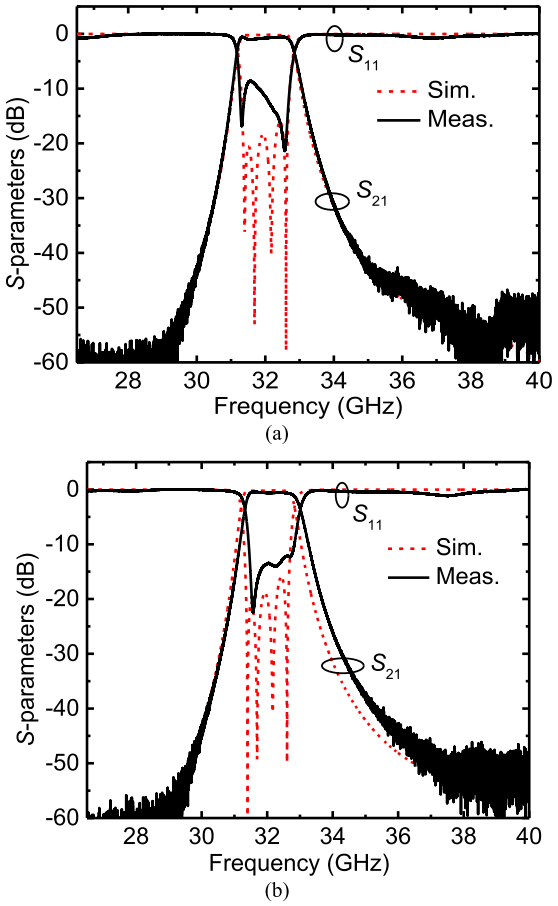

FIGURE 24. EM-simulated and RF-measured frequency responses of the *Ka*-band fourth-order hemispherical resonator BPFs. (a) Filter B. (b) Filter C.

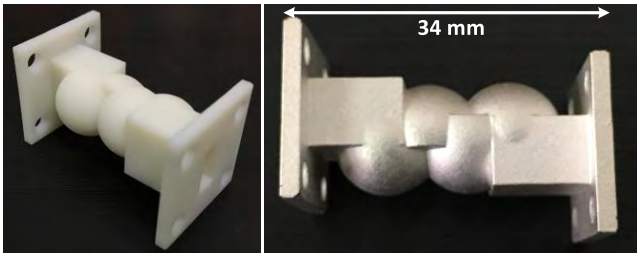

FIGURE 25. Photographs of the fabricated *Ka*-band fourth-order hemispherical resonator BPF (Filter D) before (left) and after (right) surface metallization.

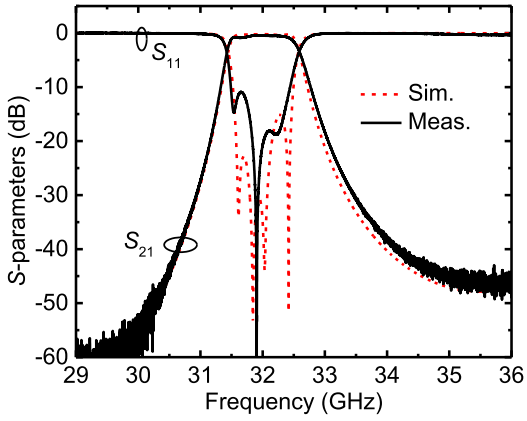

FIGURE 26. EM-simulated and RF-measured frequency responses of the *Ka*-band fourth-order hemispherical resonator BPF (Filter D).

can be investigated by measuring the surface morphology of the open-architecture hemispherical shell. The disc has a diameter of 20 mm and a thickness of 2 mm, with a good printing compatibility and a sufficient mechanical strength for testing. The hemispherical shell was designed with an inner radius of 3.8 mm that is close to the radii in Table 3. These two types of simplified samples were printed with a same printer setting (e.g., a vertical printing resolution of 50 μm) to that for the filter fabrication and were subject to the same post SLA printing process described in the Section IV A. Under such circumstance, a similar surface quality can be inspected.

The surface profile of the disc was measured before and after surface metallization by using a Veeco Dektak 150 stylus surface profiler [34] under a sampling resolution of 0.042 um. Two arbitrary and orthogonal directions (x and y) in the center region of the disc were selected for scanning, as indicated in Fig. 27(a). A linear scanning range of 1 mm was used in each direction. The discs with two different printing directions (z) were taken into consideration. The detected typical surface profiles of the disc before surface metallization are plotted in Figs. 27(b) and 27(c). For the first printing direction, the disc was placed horizontally on the board of the printer, as indicated in the inset of Fig. 27(b). For the other direction, the disc was tilted in 45° for printing, as indicated in the inset of Fig. 27(c). In the entire scanning range, the measured horizontal surface profile have peak and valley values of surface roughness of around ± 5 μm along the x and y directions. Furthermore, the surface roughness values are mostly within ± 3 μm. On the other hand, for the tilting position, larger measured values of surface roughness can be observed. The surface roughness values reach ± 9 μm and -4.2–7.7 μm along the x and y directions, respectively. The larger surface roughness is attributed to the residual edge steps of the stacked resin layers. The discs were then surface-metallized with copper and silver layers using the same electroless plating recipe described in Section IV B. The measured typical surface profiles of the metal-plated discs are plotted in Fig. 28. The peak and valley values of surface roughness are within ± 5 μm along the x and y directions for the horizontal position, and ± 10 μm and -7.7–4.3 μm along the x and y directions for the tilting position, respectively. The average surface roughness (R_a) values, defined as the arithmetic mean of the absolute values of the profile height deviations from the mean line [35], and the root mean square surface roughness (R_q) values, defined as the square root of the arithmetic mean of the squared values of the profile height deviations from the mean line [35], are summarized

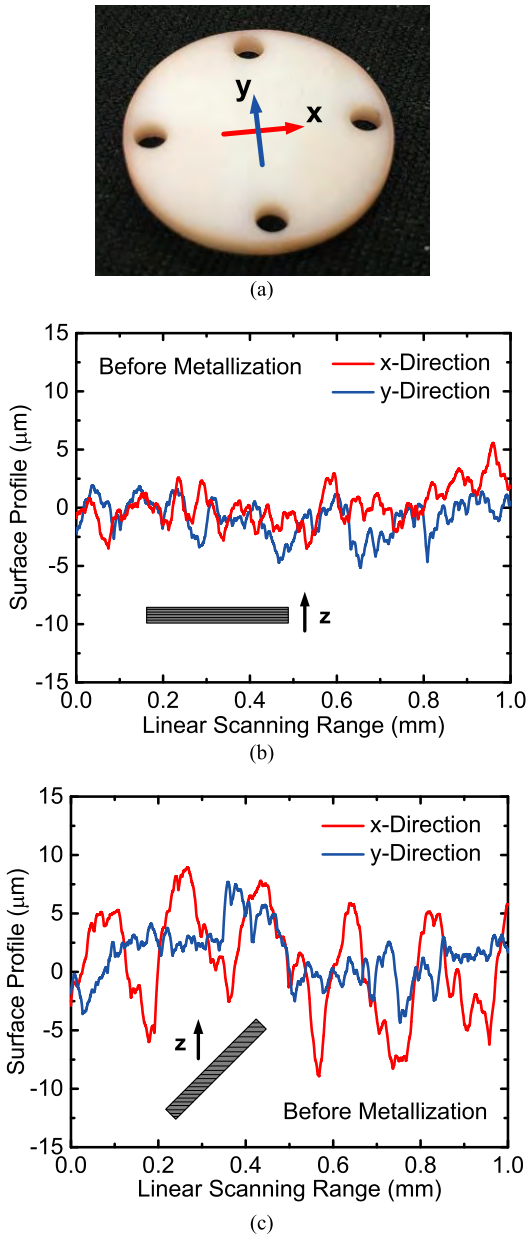

FIGURE 27. Surface profile characterization for the SLA-printed circular discs before surface metallization. (a) A graphical presentation of the sample showing the probe scanning directions. (b) Measured surface profiles for the disc that was placed horizontally for printing. (c) Measured surface profiles for the disc that was tilted in 45° for printing.

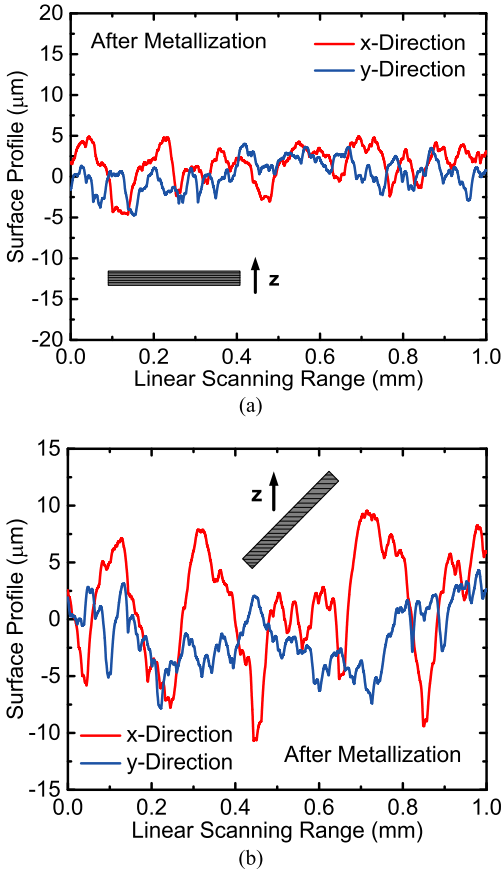

FIGURE 28. Surface profile characterization for the SLA-printed circular discs after surface metallization. (a) Measured surface profiles for the disc that was placed horizontally for printing. (b) Measured surface profiles for the disc that was tilted in 45° for printing.

TABLE 4. Calculated surface roughness of SLA-printed circular discs.

Surface Roughness (μm)	Before Plating				After Plating			
	Horizontal		Tilting		Horizontal		Tilting	
	x	*y*	*x*	*y*	*x*	*y*	*x*	*y*
R_a	1.64	1.35	3.86	2.33	1.70	1.43	3.93	2.24
R_q	2.12	1.74	4.65	2.84	2.17	1.81	4.78	2.66

in Table 4 for the aforementioned scenarios. The horizontal surface roughness values are comparable or in the same order of magnitude to the ones ($R_a = 0.93\ \mu$m and $R_q = 1.16\ \mu$m, acquired in a scanning range of 1.2 mm) for the SLA-printed Accura Xtreme resin as reported in [7]. Taking into consideration of the post plating R_a, the effective electrical conductivity of the plated copper layer was calculated in a range of (1.5–1.64) $\times\ 10^7$ S/m, which is about 25%–28% of the ideal value 5.96 $\times\ 10^7$ S/m used in the EM simulation. This degradation in the practical electrical conductivity of copper would contribute to a reduction in the hemispherical cavity's eigenmode Q_u to about 4230–4420 at 10 GHz and 2360–2470 at 32 GHz, respectively, approximately 47%–50% lower than the theoretical Q_u values discussed in Section II (see Table 1). The effect of the reduced Q_u to the filters' passband ILs are graphically compared in Fig. 29. In spite of good agreement between the RF-measured and EM-simulated ILs under degraded Q_us, it should be again noticed that the referenced R_a in Table 4 was calculated from planar surface profiles in small sampling regions, and may not perfectly represent the overall surface roughness of the practical hemispherical cavity's internal surface.

Characterization of surface morphology of the hemispherical shell was performed by using a Hitachi S-3400N-II scanning electron microscope (SEM) [36]. The hemispherical shell sample was printed in the vertical direction

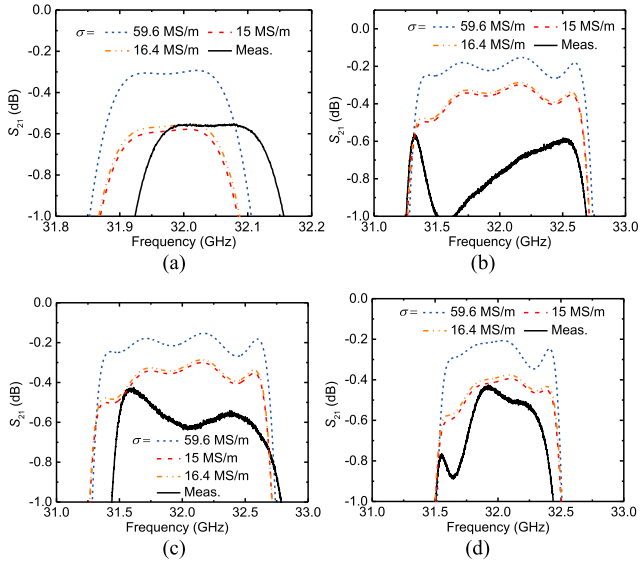

FIGURE 29. RF-measured and EM-simulated (under different Q_us) passband S_{21} parameters for the demonstrated BPFs. (a) Filter A. (b) Filter B. (c) Filter C. (d) Filter D.

as indicated in Fig. 30(a). This is in order to acquire a similar surface morphology to the one realized in the filter's cavity, under the premise of using no supporting material on the hemispherical surface. The SEM image in Fig. 30(b) shows visible edge steps of the stacked resin layers on the as-printed and unpolished hemispherical surface. The typical SEM-measured thickness of the each stacked layer is in the range of 50–70 μm. Residual ceramic particles were observed on partial regions of such surface and they are shown in Fig. 30(c). The measured particle diameter is approximately in the range of 1–10 μm. A typical resin surface after sandblasting and manual polishing is shown in Fig. 30(d), where traces of the edge steps and ceramic particles are removed and a relatively smooth surface is obtained. However, for the demonstrated filters, the inner surface of the hemispherical cavity cannot be polished as well as the shell discussed in this Section. Therefore, the practical filters suffer from the conductive loss because of the inner surface roughness.

A comparison in the SEM-inspected surface morphologies for the disc samples is graphically represented in Fig. 31. For the disc printed in the tilting position, a periodical step profile can be observed [Fig. 31(a)] even though the surface was manually polished, whereas for the polished disc that was printed in the horizontal position, a relatively smooth profile can be seen [Fig. 31(b)]. Lastly, the surface grains of the electroless plated silver layer is shown in Fig. 32.

Finally, a quantitative comparison in the major specifications for the filters of this work to those of the state of the art is summarized in Table 5. It demonstrates that—1. the filters of this work achieve in the passbands small frequency shifts (0.01%–0.47%) as well as good transmission

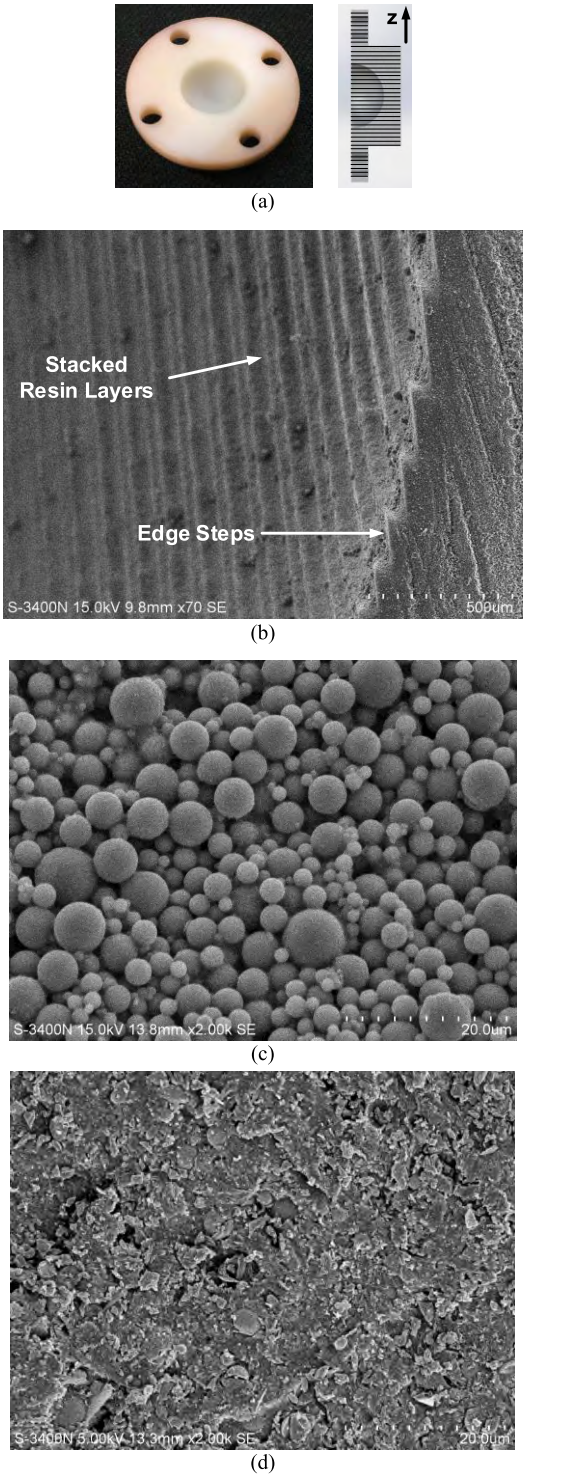

FIGURE 30. Characterization of surface morphology for the SLA-printed hemispherical shells. (a) A graphical presentation of the tested sample indicating the printing direction. (b) The SEM image of the as-printed and unpolished resin surface containing edge steps of the stacked resin layers. (c) The SEM image of the residual ceramic particles. (d) The SEM image of the resin surface after sandblasting and manual polishing.

and reflection coefficients that are better or comparable to previous works reported in literature; 2. the monolithic realization for the relatively small and enclosed architectures of

TABLE 5. Comparison with state-of-the-art SLA-printed microwave/millimeter-wave BPFs.

References	f_0 (GHz)	FBW	Filter Order	RL (dB)	IL (dB)	Δf^*(%)	High-Temperature Operability	Monolithic SLA Printing	Sidewall Openings	Plating Techniques
[7]	107.2	6.3%	6	>11	0.95	7.2	—	—	—	EP Cu
[10]	19.65	1.2%	4	>10	1.7	0.15	—	—	—	EP Cu
[11]	0.5	4%	4	>15	0.9	N/A	—	—	—	EP Cu
[12]	10	5%	5	>20	0.11	0.05	—	—	—	EP Cu
[13]	10	3%	4	>18	0.24	0.01	—	Yes	Yes	EP Cu
[14]	87.5	11.5%	5	>18	0.3–0.5	2.78	—	Yes	Yes	EP Cu/Au
[15]	10	3%	4	>17	0.24	0.8	Yes	Yes	Yes	EP Cu
[21]	32.2	13.6%	5	>17	0.23–0.5	0.37	Yes	Yes	Yes	EP Cu/ELP Ag
T.W. Filter A	32	1%	2	>17	0.56–0.7	0.04	Yes	Yes	—	ELP Cu/Ag
T.W. Filter B	32.01	5%	4	>10	0.58–1	0.01	Yes	Yes	—	ELP Cu/Ag
T.W. Filter C	32.17	5%	4	>12	0.43–1	0.47	Yes	Yes	—	ELP Cu/Ag
T.W. Filter D	32	3%	4	>11	0.43–0.9	0.06	Yes	Yes	—	ELP Cu/Ag

*T.W.: This work; Δf: Center frequency shift; EP: Electroplating; ELP: Electroless plating; N/A: Not available.

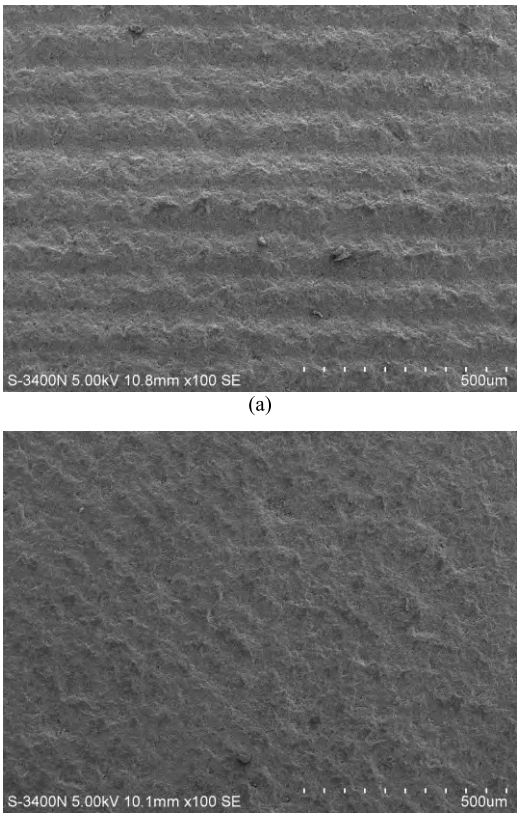

FIGURE 31. Surface morphology for the SLA-printed circular discs. The resin surface has been sandblasted and polished. (a) The SEM image of the resin surface that was tilted in 45° for printing. (b) The SEM image of the resin surface that was placed horizontally for printing.

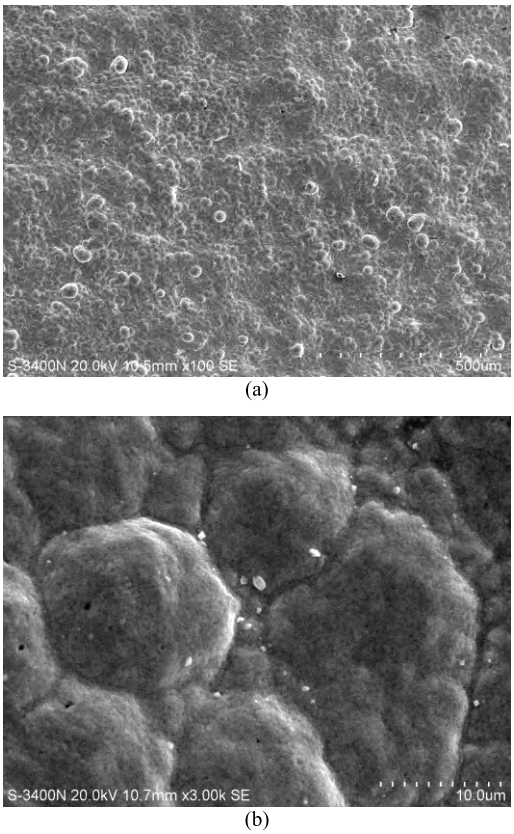

FIGURE 32. Surface morphology for the metal-plated disc. (a) The SEM image of the electroless plated silver surface. (b) The zoom-in SEM image of the silver surface grain.

this work indicates a high accuracy and reliability of the proprietary SLA printing and barrel electroless plating techniques that are comparable to the state of the art developed by Swissto12® Company [37]. The proposed filters not only perform similar transfer functions to conventional rectangular waveguide filters of the same orders, but also benefit from highly integrated coupling structures that are more compact (almost 50% smaller in length) than the latter.

VII. CONCLUSION

This paper presents a comprehensive study on the hemispherical resonator and the constituent millimeter-wave BPFs that are practically implemented using cost-efficient SLA-based AM and particularly optimized electroless nickel/

copper/silver plating techniques. The paper offers technical contributions in following aspects—1). a detailed theoretical analysis of the hemispherical resonator including EM field distribution of resonant modes and analytical calculation for the resonant frequency and the Q_u; 2). novel designs of second- and fourth-order hemispherical resonator BPFs with flexible and compact coupling configurations that provide a significant improvement in the filters' out-of-band rejections (e.g., over 40 dB at 34−40 GHz); 3). monolithic, low-cost, and high-performance realizations of the proof-of-concept *Ka*-band filter prototypes with combination of the proprietary SLA printing and barrel electroless plating techniques. The work demonstrates good RF performance (e.g., frequency shifts as small as 0.01%–0.47%, ILs: 0.43−1 dB, and RLs: mostly >10−17 dB) of the manufactured *Ka*-band filters, which validates a high accuracy and reliability of the developed fabrication processes. Furthermore, it evidences the possibility of a monolithic integration for geometrically complicated and architecture-enclosed microwave waveguide devices without the need of either split-block designs or sidewall openings. This can be one of promising trends worth future research and development in the area of polymer-based AM of microwave and millimeter-wave devices.

ACKNOWLEDGMENT

The authors thank Mr. X. Wu for the assistance in measuring the surface profiles, and College of Chemistry and Environment Engineering, Shenzhen University, and Harbin Institute of Technology, Shenzhen, for offering access to measurement facilities for characterization of the surface morphology.

REFERENCES

[1] F. Calignano *et al.*, "Overview on additive manufacturing technologies," *Proc. IEEE*, vol. 105, no. 4, pp. 593–612, Apr. 2017.

[2] T.-H. Chio, G.-L. Huang, and S.-G. Zhou, "Application of direct metal laser sintering to waveguide-based passive microwave components, antennas, and antenna arrays," *Proc. IEEE*, vol. 105, no. 4, pp. 632–644, Apr. 2017.

[3] O. A. Peverini *et al.*, "Selective laser melting manufacturing of microwave waveguide devices," *Proc. IEEE*, vol. 105, no. 4, pp. 620–631, Apr. 2017.

[4] B. Zhang, Y.-X. Guo, H. Zirath, and Y. P. Zhang, "Investigation on 3-D-printing technologies for millimeter-wave and terahertz applications," *Proc. IEEE*, vol. 105, no. 4, pp. 723–736, Apr. 2017.

[5] A. I. Dimitriadis *et al.*, "Polymer-based additive manufacturing of high-performance waveguide and antenna components," *Proc. IEEE*, vol. 105, no. 4, pp. 668–676, Apr. 2017.

[6] A. von Bieren, E. de Rijk, J.-P. Ansermet, and A. Macor, "Monolithic metal-coated plastic components for mm-wave applications," in *Proc. 39th Int. Conf. Infr., Millim., Terahertz Waves*, Tucson, AZ, USA, Sep. 2014, pp. 1–2.

[7] M. D'Auria *et al.*, "3-D printed metal-pipe rectangular waveguides," *IEEE Trans. Compon. Packag. Manuf. Technol.*, vol. 5, no. 9, pp. 1339–1349, Sep. 2015.

[8] J. Shen *et al.*, "Rapid prototyping of low loss 3D printed waveguides for millimeter-wave applications," in *IEEE MTT-S Int. Microw. Symp. Dig.*, Honolulu, HI, USA, Jun. 2017, pp. 41–44.

[9] J. Shen, M. Aiken, C. Ladd, M. D. Dickey, and D. S. Ricketts, "A simple electroless plating solution for 3D printed microwave components," in *Proc. Asia–Pacific Microw. Conf.*, New Delhi, India, Dec. 2016, pp. 1–4.

[10] B. Liu, X. Gong, and W. J. Chappell, "Applications of layer-by-layer polymer stereolithography for three-dimensional high-frequency components," *IEEE Trans. Microw. Theory Techn.*, vol. 52, no. 11, pp. 2567–2575, Nov. 2004.

[11] X. Shang, J. Li, C. Guo, M. J. Lancaster, and J. Xu, "3-D printed filter based on helical resonators with variable width," in *IEEE MTT-S Int. Microw. Symp. Dig.*, Honolulu, HI, USA, Jun. 2017, pp. 1587–1590.

[12] C. Guo, X. Shang, M. J. Lancaster, and J. Xu, "A 3-D printed lightweight X-band waveguide filter based on spherical resonators," *IEEE Microw. Wireless Compon. Lett.*, vol. 25, no. 7, pp. 442–444, Jul. 2015.

[13] C. Guo, X. Shang, J. Li, F. Zhang, M. J. Lancaster, and J. Xu, "A lightweight 3-D printed X-band bandpass filter based on spherical dual-mode resonators," *IEEE Microw. Wireless Compon. Lett.*, vol. 26, no. 8, pp. 568–570, Aug. 2016.

[14] X. Shang *et al.*, "*W*-band waveguide filters fabricated by laser micromachining and 3-D printing," *IEEE Trans. Microw. Theory Techn.*, vol. 64, no. 8, pp. 2572–2580, Aug. 2016.

[15] C. Guo, J. Li, D. D. Dinh, X. Shang, M. J. Lancaster, and J. Xu, "Ceramic filled resin based 3D printed *X*-band dual-mode bandpass filter with enhanced thermal handling capability," *Electron. Lett.*, vol. 52, no. 23, pp. 1929–1931, Nov. 2016.

[16] M. Dionigi, C. Tomassoni, G. Venanzoni, and R. Sorrentino, "Simple high-performance metal-plating procedure for stereolithographically 3-D-printed waveguide components," *IEEE Microw. Wireless Compon. Lett.*, vol. 27, no. 11, pp. 953–955, Nov. 2017.

[17] P. T. Timbie, J. Grade, D. van der Weide, B. Maffei, and G. Pisano, "Stereolithographed MM-wave corrugated horn antennas," in *Proc. Int. Conf. Infr., Millim. Terahertz Waves*, Houston, TX, USA, Oct. 2011, pp. 1–3.

[18] G. P. Le Sage, "3D printed waveguide slot array antennas," *IEEE Access*, vol. 4, pp. 1258–1265, 2016.

[19] J. S. Silva, M. García-Vigueras, T. Debogović, J. R. Costa, C. A. Fernandes, and J. R. Mosig, "Stereolithography-based antennas for satellite communications in Ka-band," *Proc. IEEE*, vol. 105, no. 4, pp. 655–667, Apr. 2017.

[20] X. Shang, P. Klasmann, and M. J. Lancaster, "A compact Ka-band waveguide orthomode transducer fabricated by 3-D printing," in *Proc. Eur. Microw. Conf.*, London, U.K., Oct. 2016, pp. 365–368.

[21] J. Li, C. Guo, J. Xu, and L. Mao, "Lightweight low-cost Ka-band 3-D printed slotted rectangular waveguide bandpass filters," in *Proc. IEEE Int. Symp. Antennas Propag.*, San Diego, CA, USA, Jul. 2017, pp. 2647–2648.

[22] K. Zhang and D. Li, *Electromagnetic Theory for Microwaves and Optoelectronics*, 2nd ed. Berlin, Germany: Springer-Verlag, 2008.

[23] CST Computer Simulation Technology AG., USA. (Jul. 2017). [Online]. Available: https://www.cst.com

[24] MathWorks, Inc., Natick, MA, USA, (Mar. 2018). *MATLAB*. [Online]. Available: https://www.mathworks.com

[25] R. A. Yadav and I. D. Singh, "Normal modes and quality factors of spherical dielectric resonators: I—Shielded dielectric sphere," *Pramana*, vol. 62, no. 6, pp. 1255–1271, Jun. 2004.

[26] J.-S. G. Hong and M. J. Lancaster, *Microstrip Filters for RF/Microwave Applications*. New York, NY, USA: Wiley, 2001.

[27] (Jun. 2017). *Shanghai New East China Institute of Photoelectric Technology*. [Online]. Available: https://www.shplasma.com

[28] Somos. (Sep. 2016). *Stereolithography Materials*. [Online]. Available: https://www.dsm.com

[29] (Jun. 2016). *Accura Xtreme*. [Online]. Available: https://www.3dsystems.com

[30] C. Guo *et al.*, "Novel microwave/millimeter-wave passive waveguide devices based on 3-D printing techniques," *J. Infr. Millim. Waves*, vol. 36, no. 1, pp. 81–91, Feb. 2017.

[31] Keysight Technologies, Inc., (Oct. 2016). [Online]. Available: https://www.keysight.com

[32] W. L. Wang, C. M. Cheah, J. Y. H. Fuh, and L. Lu, "Influence of process parameters on stereolithography part shrinkage," *Mater. Des.*, vol. 17, no. 4, pp. 205–213, 1996.

[33] Q. Huang, J. Zhang, A. Sabbaghi, and T. Dasgupta, "Optimal offline compensation of shape shrinkage for three-dimensional printing processes," *IIE Trans.*, vol. 47, no. 5, pp. 431–441, 2015.

[34] Veeco Instruments, Inc. (May 2018). *Veeco Dektak 150 Surface Profiler*. [Online]. Available: https://www.veeco.com
[35] *Assessment of Surface Texture. Guidance and General Information*, BSI Standards BS 1134:2010, 2010.
[36] Hitachi, Ltd. (May 2018). *Hitachi S-3400N-II Scanning Electron Microscope*, [Online]. Available: https://www.hitachi.com
[37] Swissto12 SA, (Mar. 2018). [Online]. Available: https://www.swissto12.com

JIN LI (S'11–M'17) received the B.E. degree in electronic information engineering and the Ph.D. degree in radio physics from the University of Electronic Science and Technology of China, Chengdu, Sichuan, China, in 2010 and 2017, respectively.

He was a Visiting Research Scholar with the Birck Nanotechnology Center, School of Electrical and Computer Engineering, Purdue University, West Lafayette, IN, USA, from 2013 to 2015, supported by the China Scholarship Council under the State Scholarship Fund. Since 2017, he has been an External Research Specialist with the ATR National Key Laboratory of Defense Technology, College of Information Engineering, Shenzhen University, Shenzhen, Guangdong, China, where he is currently a Post-Doctoral Research Fellow. His current research interests include the RF design and characterization of reconfigurable microwave filters, microwave and millimeter-wave passive components, RF microelectromechanical systems, thin-film materials, and additive manufacturing.

Dr. Li is a member of the IEEE Microwave Theory and Techniques Society (IEEE MTT-S), the Chinese Institute of Electronics, and the Applied Computational Electromagnetics Society. He was a co-recipient of the First Place Award at the 2014 and 2015 IEEE MTT-S International Microwave Symposium Tunable RF-MEMS Filter Student Design Competitions. He is a Reviewer for several international journals, including the IEEE Access, the IEEE Microwave and Wireless Components Letters, and *Electronics Letters*.

CHENG GUO received the B.E. degree in communication engineering from Southwest Jiaotong University and the Ph.D. degree in radio physics from the University of Electronic Science and Technology of China in 2012 and 2016, respectively.

From 2014 to 2016, he was a Visiting Ph.D. Student with the Department of Electronic, Electrical and Systems Engineering, University of Birmingham, Edgbaston, Birmingham, U.K., where he has been a Post-Doctoral Research Fellow since 2017. His current research interests include 3-D printing of passive microwave devices and Schottky-diode-based terahertz frequency multipliers and mixers.

Dr. Guo was a co-recipient of the IEEE MTT-S Tatsuo Itoh Award in 2017. He is a Reviewer for several international journals, including the IEEE Transactions on Microwave Theory and Techniques, the IEEE Microwave and Wireless Components Letters, the IEEE Access, and *Electronics Letters*.

LIJIAN MAO received the B.E. degree in inorganic chemical engineering from the Tianjin University of Science and Technology, Tianjin, China, in 1993.

He was an Engineer with the Wynca Group, Zhejiang, China, from 1993 to 1997, Gul Technologies Singapore Pte., Ltd., Singapore, from 1997 to 2000, and Gultech (Suzhou) Electronics Co., Ltd., Suzhou, Jiangsu, China, from 2000 to 2003. He was the Manager with the Division of Electroplating, Molex, Shanghai, China, from 2003 to 2010, and the Technical Director with Shanghai Reetu Surface Treatment Co., Ltd., from 2010 to 2016. He is currently with Kunshan Tongxin Surface Science and Technology Co., Ltd., Kunshan, Jiangsu, China.

JIE XIANG received the B.E. degree in mechanical design and machine automation from Anhui Polytechnic University, Wuhu, Anhui, China, in 2008.

From 2008 to 2014, he was with the Precision Manufacturing Division, Process Group, East China Photoelectric Technology Research Institute (ECPTRI), Wuhu. He was involved in the documentation and the development of fabrication process for microwave traveling-wave tubes and microwave solid-state amplifiers. From 2014 to 2017, he was the Deputy General Manager of the Anhui Xinwu Research Institute of Precise Equipment Manufacture and Applications, Wuhu, where he was involved in the research and development of 3-D printing techniques and industrial-grade stereolithography printers. He was also involved in the foundation of the 3-D printing center offering worldwide services in high-precision manufacturing, 3-D printing recipe optimization, and post fabrication process. Since 2017, he has been the Director of the Plasma Gasification Division, Shanghai New East China Institute of Optoelectronic Technology, Shanghai, China. His current research interests include precise fabrication process for microwave devices, electric arc and microwave plasma techniques for garbage disposal, and 3-D printing of customized engineering structures.

He holds seven Chinese patents. He received the Outstanding Staff Award from ECPTRI in 2009, 2010, and 2013, respectively. He was a recipient of the Third Place Award at the Wuhu First Innovation and Entrepreneurship Competition in 2015.

GUAN-LONG HUANG (M'11) received the B.E. degree in electronic information engineering from the Harbin Institute of Technology, Harbin, China, and the Ph.D. degree in electrical and computer engineering from the National University of Singapore, Singapore.

He was with Temasek Laboratories, National University of Singapore, as a Research Scientist, and Nokia Solutions and Networks System Technology as a Senior Antenna Specialist from 2011 to 2017. He is currently an Assistant Professor with the ATR National Key Laboratory of Defense Technology, College of Information Engineering, Shenzhen University, Shenzhen, Guangdong, China. He also serves as the Deputy Director of the Guangdong Provincial Mobile Terminal Microwave and Millimeter-Wave Antenna Engineering Research Center. His research interests include the design and implementation of planar antenna arrays, 5G base stations, mobile RF front-end devices, phased antenna arrays, channel coding for massive MIMO applications, and 3-D printing technology in microwave applications.

Dr. Huang is currently serving as an Associate Editor for the journal IEEE Access.

TAO YUAN received the B.E. and M.E. degrees from Xidian University, China, and the Ph.D. degree from the National University of Singapore, Singapore.

He is currently a Professor with the College of Information Engineering, Shenzhen University, Shenzhen, Guangdong, China. His current research interests include the development of novel RF modules and antennas for mobile terminals and 5G applications.